STATE OF THE CLIMATE IN 2021

ANTARCTICA AND THE SOUTHERN OCEAN

K. R. Clem and M. N. Raphael, Eds.

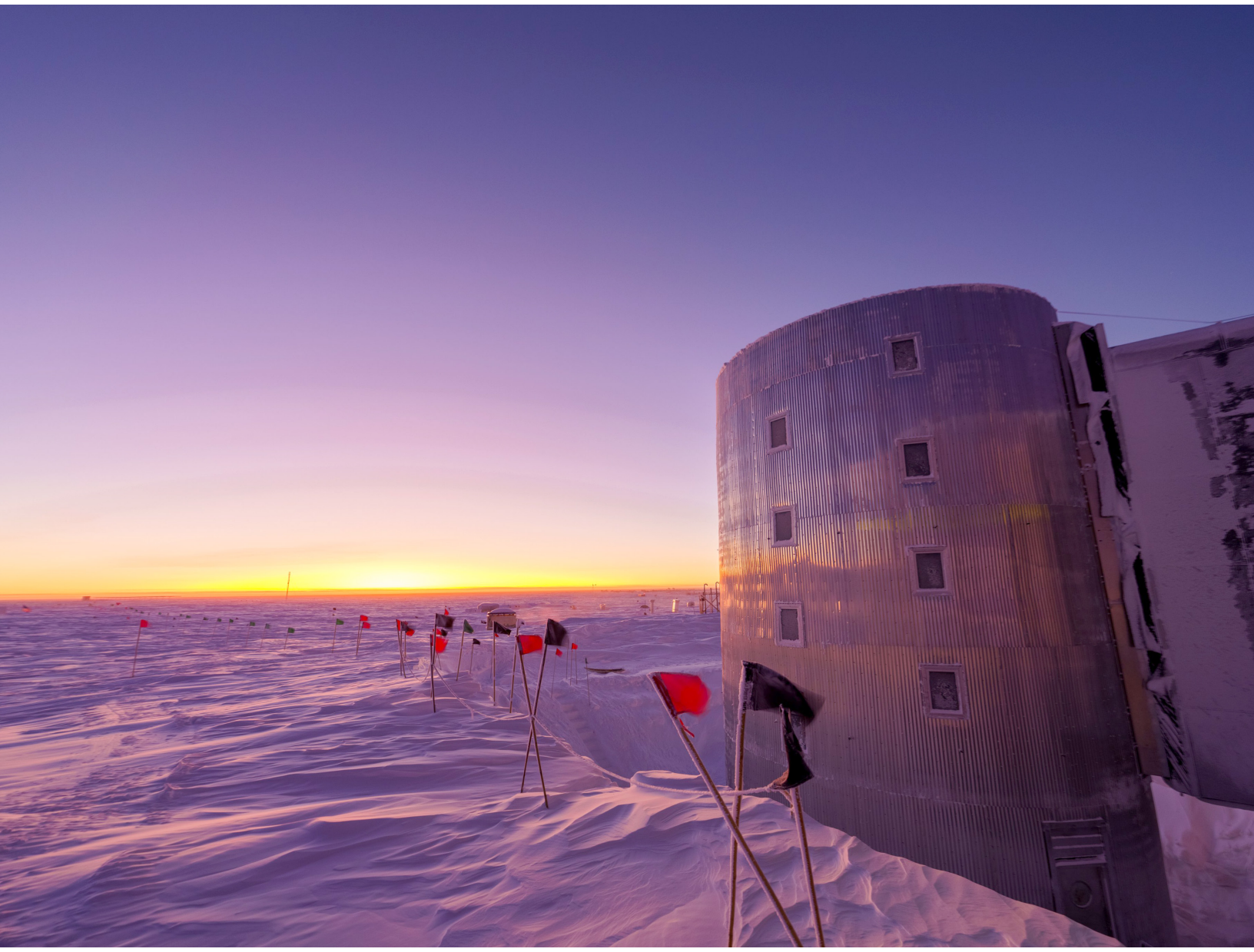

Special Online Supplement to the *Bulletin of the American Meteorological Society*, Vol. 103, No. 8, August 2022

https://doi.org/10.1175/BAMS-D-22-0078.1

Corresponding author: Kyle R. Clem / kyle.clem@vuw.ac.nz

STATE OF THE CLIMATE IN 2021

Antarctica and the Southern Ocean

Editors

Jessica Blunden
Tim Boyer

Chapter Editors

Freya Aldred
Peter Bissolli
Kyle R. Clem
Howard J. Diamond
Matthew L. Druckenmiller
Robert J. H. Dunn
Catherine Ganter
Nadine Gobron
Gregory C. Johnson
Rick Lumpkin
Ademe Mekonnen
John B. Miller
Twila A. Moon
Marilyn N. Raphael
Ahira Sánchez-Lugo
Carl J. Schreck III
Richard L. Thoman
Kate M. Willett
Zhiwei Zhu

Technical Editor

Laura Ohlmann

BAMS Special Editor for Climate

Michael A. Alexander

American Meteorological Society

Cover credit:
Photograph taken at the South Pole in 2021 by Jeffrey Keller, USAP/PAE, Preventative Manitenance Foreman, Colorado Springs, Colorado.

Antarctica and the Southern Ocean is one chapter from the *State of the Climate in 2021* annual report and is available from https://doi.org/10.1175/BAMS-D-22-0078.1. Compiled by NOAA's National Centers for Environmental Information, *State of the Climate in 2021* is based on contributions from scientists from around the world. It provides a detailed update on global climate indicators, notable weather events, and other data collected by environmental monitoring stations and instruments located on land, water, ice, and in space. The full report is available from 10.1175/2022BAMSStateoftheClimate.1.

How to cite this document:

Citing the complete report:
Blunden, J. and T. Boyer, Eds., 2022: "State of the Climate in 2021". *Bull. Amer. Meteor. Soc.,* **103** (8), Si–S465, https://doi.org/10.1175/2022BAMSStateoftheClimate.1

Citing this chapter:
Clem, K. R. and M. N. Raphael, Eds., 2022: Antarctica and the Southern Ocean [in "State of the Climate in 2021"]. *Bull. Amer. Meteor. Soc.*, **103** (8), S307–S340, https://doi.org/10.1175/BAMS-D-22-0078.1.

Citing a section (example):
Reid, P., S. Stammerjohn, R. A. Massom, S. Barreira, T. Scambos, and J. L. Lieser, 2022: Sea ice extent, concentration, and seasonality [in "State of the Climate in 2021"]. *Bull. Amer. Meteor. Soc.*, **103** (8), S325–S329, https://doi.org/10.1175/BAMS-D-21-0078.1.

Editor and Author Affiliations (alphabetical by name)

Adusumilli, Susheel, Scripps Institution of Oceanography, University of California San Diego, La Jolla, California

Baiman, Rebecca, Department of Atmospheric and Oceanic Sciences, University of Colorado Boulder, Boulder, Colorado

Banwell, Alison F., Earth Science and Observation Center, CIRES, University of Colorado, Boulder, Colorado

Barreira, Sandra, Argentine Naval Hydrographic Service, Buenos Aires, Argentina

Beadling, Rebecca L., NOAA, Geophysical Fluid Dynamics Laboratory, Princeton University Atmospheric and Oceanic Sciences Program, Princeton, New Jersey and University Corporation for Atmospheric Research, Boulder, Colorado

Clem, Kyle R., School of Geography, Environment and Earth Sciences, Victoria University of Wellington, Wellington, New Zealand

Colwell, Steve, British Antarctic Survey, Cambridge, United Kingdom

Coy, Lawrence, Science Systems and Applications, Inc., Lanham, Maryland, and NASA Goddard Space Flight Center, Greenbelt, Maryland

Datta, Rajashree T., Department of Atmospheric and Oceanic Sciences, University of Colorado Boulder, Boulder, Colorado

De Laat, Jos, Royal Netherlands Meteorological Institute (KNMI), DeBilt, Netherlands

Dunmire, Devon, Department of Atmospheric and Oceanic Sciences, University of Colorado Boulder, Boulder, Colorado

Fogt, Ryan L., Department of Geography, Ohio University, Athens, Ohio

Freeman, Natalie M., Department of Atmospheric and Oceanic Sciences, University of Colorado Boulder, Boulder, Colorodo

Fricker, Helen Amanda, Scripps Institution of Oceanography, University of California San Diego, La Jolla, California

Gardner, Alex S., Jet Propulsion Laboratory, California Institute of Technology, Pasadena, California

Johnson, Bryan, NOAA/OAR Earth System Research Laboratory, Global Monitoring Division, and University of Colorado Boulder, Boulder, Colorado

Keller, Linda M., Department of Atmospheric and Oceanic Sciences, University of Wisconsin-Madison, Madison, Wisconsin

Kramarova, Natalya A., NASA Goddard Space Flight Center, Greenbelt, Maryland

Lazzara, Matthew A., Department of Physical Sciences, School of Arts and Sciences, Madison Area Technical College, and Space Science and Engineering Center, University of Wisconsin-Madison, Madison, Wisconsin

Lieser, Jan L., Australian Bureau of Meteorology and Institute for Marine and Antarctic Studies (IMAS), University of Tasmania, Hobart, Tasmania, Australia

MacFerrin, Michael, Earth Science and Observation Center, CIRES, University of Colorado, Boulder, Colorado

MacGilchrist, Graeme A., NOAA, Geophysical Fluid Dynamics Laboratory, and Princeton University Atmospheric and Oceanic Sciences Program, Princeton, New Jersey

MacLennan, Michelle L., Department of Atmospheric and Oceanic Sciences, University of Colorado Boulder, Boulder, Colorado

Massom, Robert A., Australian Antarctic Division, Australian Antarctic Program Partnership (AAPP) and Australian Centre for Excellence in Antarctic Science (ACEAS), Hobart, Tasmania, Australia

Mazloff, Matthew R., Scripps Institution of Oceanography, University of California, San Diego, La Jolla, California

Mote, Thomas L., Department of Geography, University of Georgia

Nash, Eric R., Science Systems and Applications, Inc., Lanham, Maryland, and NASA Goddard Space Flight Center, Greenbelt, Maryland

Newman, Paul A., NASA Goddard Space Flight Center, Greenbelt, Maryland

Norton, Taylor, Department of Atmospheric and Oceanic Sciences, University of Wisconsin-Madison, Madison, Wisconsin

Petropavlovskikh, Irina, NOAA/OAR Earth System Research Laboratory, Global Monitoring Division, and University of Colorado Boulder, Boulder, Colorado

Pitts, Michael, NASA Langley Research Center, Hampton, Virginia

Raphael, Marilyn N., Department of Geography, University of California-Los Angeles, Los Angeles, California

Reid, Phillip, Australian Bureau of Meteorology and Australian Antarctic Program Partnership (AAPP), Hobart, Tasmania, Australia

Santee, Michelle L., NASA Jet Propulsion Laboratory, Pasadena, California

Scambos, Ted A., Earth Science and Observation Center, CIRES, University of Colorado, Boulder, Colorado

Shi, Jia-Rui, Woods Hole Oceanographic Institution, Woods Hole, Massachusetts

Stammerjohn, Sharon, Institute of Arctic and Alpine Research, University of Colorado, Boulder, Colorado

Strahan, Susan E., University of Maryland Baltimore County, Baltimore, Maryland, and NASA Goddard Space Flight Center, Greenbelt, Maryland

Thompson, Andrew F., Environmental Science and Engineering, California Institute of Technology, Pasadena, California

Wille, Jonathan D., Institut des Géosciences de l'Environnement, CNRS/UGA, Saint Martin d'Hères, France

Wilson, Earle, Environmental Science and Engineering, California Institute of Technology, Pasadena, California

Editorial and Production Team

Allen, Jessicca, Graphics Support, Cooperative Institute for Satellite Earth System Studies, North Carolina State University, Asheville, North Carolina

Hammer, Gregory, Content Team Lead, Communications and Outreach, NOAA/NESDIS National Centers for Environmental Information, Asheville, North Carolina

Love-Brotak, S. Elizabeth, Lead Graphics Production, NOAA/NESDIS National Centers for Environmental Information, Asheville, North Carolina

Misch, Deborah J., Graphics Support, Innovative Consulting and Management Services, LLC, NOAA/NESDIS National Centers for Environmental Information, Asheville, North Carolina

Ohlmann, Laura, Technical Editor, Innovative Consulting and Management Services, LLC, NOAA/NESDIS National Centers for Environmental Information, Asheville, North Carolina

Riddle, Deborah B., Graphics Support, NOAA/NESDIS National Centers for Environmental Information, Asheville, North Carolina

Veasey, Sara W., Visual Communications Team Lead, Communications and Outreach, NOAA/NESDIS National Centers for Environmental Information, Asheville, North Carolina

6. Table of Contents

*Please refer to Chapter 8 (Relevant datasets and sources) for a list of all climate variables and datasets used in this chapter for analyses, along with their websites for more information and access to the data.

6. ANTARCTICA AND THE SOUTHERN OCEAN

K. R. Clem and M. N. Raphael, Eds..

a. Overview—K. R. Clem and M. N. Raphael

Antarctica and the Southern Ocean were dominated by below-average pressure and stronger than average circumpolar westerly winds through much of 2021, resulting in many new low-pressure records set across the continent. The low pressure that gripped the polar cap extended vertically through the troposphere and stratosphere and was accompanied by a persistently strong and stable polar vortex. This helped deliver the coldest winter on record to the South Pole (see Sidebar 6.1) and also helped maintain one of the longest-lived ozone holes on record (second only to the 2020 ozone hole), which did not close until 23 December. Despite the long duration of the ozone hole, its size and the minimum ozone concentrations did not reach exceptional levels, and its slow growth rate in 2021 is consistent with ongoing recovery trends.

Embedded within the low pressure over the polar cap were several strong regional cyclonic circulations that produced marked anomalies in all aspects of the coupled climate system. In particular, the Amundsen Sea Low was stronger than normal through most of the year. This brought persistent warm northerly winds to the Antarctic Peninsula (AP) and the surrounding Bellingshausen and western Weddell Seas regions (see Fig. 6.1 for map). Esperanza and Marambio stations on the northeastern Peninsula experienced their warmest (tied) and second warmest years on record, respectively; sea ice concentration and extent in the Bellingshausen and western Weddell Seas remained well below average through most of the year. The annual surface mass balance (accumulated precipitation minus sublimation/surface meltwater runoff) was over 25% higher than average on the Peninsula, while surface melt was also above average, particularly across the Larsen C and remnant Larsen B ice shelves, where there were more than 30 days above the average number of surface melt days during the 2020/21 melt season. Meanwhile, strong storms and turbulent conditions brought near-record high ocean mixed layer depth and salinity across the southeast South Pacific, which contributed to the second highest chlorophyll concentration and phytoplankton growth on record for this region in January 2021.

Strong, regional, cyclonic anomalies were also seen near Dronning Maud Land (~30°W–30°E) and Wilkes Land (~90°–120°E). These helped trigger and guide a higher-than-normal number of landfalling atmospheric rivers into these regions, particularly during October in Wilkes Land and December in Dronning Maud Land. This resulted in an annual surface mass balance that was over 50% above average in both regions for 2021.

Despite the higher-than-normal surface mass gains in several regions, Antarctica as a whole continued to lose mass in 2021. A net mass loss of 50 Gt occurred from December 2020 to December 2021 (~0.14 mm of global sea level rise), almost all of which came from the coastal margins of West Antarctica where there was also a continued decrease in surface elevation. However, the mass loss in 2021 was far less than the average rate of annual mass loss of 140 Gt yr^{-1} since 2003, suggesting a major positive contribution of surface processes to seasonal mass and height changes. Despite such large regional surface mass gains, the loss of ice from the West Antarctic Ice Sheet (WAIS) continued to overwhelm gains from surface accumulation, and Antarctica continued its ongoing contribution to global sea level rise in 2021.

Antarctic sea ice anomalies exhibited dramatic seasonal variability, similar to that seen in recent years. The year began with below-average overall sea ice extent in January and February,

before abruptly switching to above average in late February; the above-average conditions persisted until September, reaching near-record high daily extents in August. Following an anomalously early daily maximum extent on 30 August, sea ice then retreated rapidly from September to December, with sea ice area plummeting to record low daily values in parts of October and December. A new monthly mean record-low sea ice area was set in December 2021.

More details on Antarctica's climate and cryosphere, the Southern Ocean, and the ozone hole for 2021 are presented in this chapter. In most cases, where data are available, 2021 anomalies are based on the 1991–2020 climatological average. Otherwise, the climatological period is provided within each section. The geographical locations of place names mentioned throughout the Chapter are provided in Fig. 6.1.

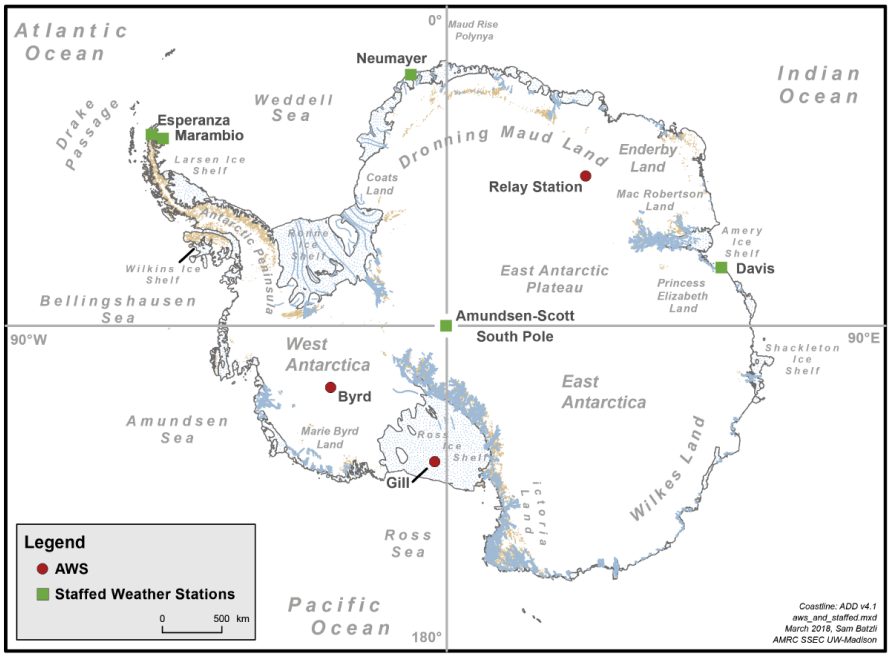

Fig. 6.1. Map of the automated (AWS) and staffed weather stations and regions discussed in this chapter. Light brown areas are rock exposures on the Antarctic continent; blue stippling indicates ice shelf areas, but in areas of heavy crevassing on both the ice shelves and the ice sheet, the surface is shown in solid gray-blue on the map. A few selected flow line features and shear margins are shown as blue lines.

b. Atmospheric circulation and surface observations—K. R. Clem, S. Barreira, R. L. Fogt, S. Colwell, L. M. Keller, M. A. Lazzara, and T. Norton

Much of continental Antarctica experienced below-average surface pressure during 2021, which was accompanied by predominantly positive phases of the Southern Annular Mode (SAM; the leading mode of extratropical Southern Hemisphere atmospheric circulation; the positive phase reflects above-average pressure in the middle latitudes and below-average pressure over Antarctica). Many negative pressure records were set across the continent throughout the year, with the strongest negative pressure anomalies occurring during December in the Antarctic Peninsula, West Antarctica, and the Ross Ice Shelf region; no positive pressure records were set in Antarctica during 2021. Surface pressure was also well below average in the Amundsen and Bellingshausen Seas for most of the year, reflecting an anomalously deep Amundsen Sea Low, which is consistent with the South Pacific atmospheric circulation response to the La Niña conditions that persisted through much of 2021 (Turner et al. 2013; see section 4b). The atmospheric circulation anomalies produced anomalously warm conditions across the Antarctic Peninsula for most of the year, with Esperanza tying 2016 for its warmest year on record and Marambio recording its second-warmest year on record behind 2016 (both located on the northeast Peninsula). Parts of the interior, especially the South Pole region into Dronning Maud Land, experienced the coldest winter on record (see Sidebar 6.1 for details), while conversely the remainder of East Antarctica experienced a slightly warmer-than-average year (around 1°C above average) due to localized warm advection from a persistent regional cyclonic anomaly near the Amery Ice Shelf. Above the surface, geopotential height and temperature over the polar cap were generally below average in the upper troposphere and stratosphere throughout the year, especially during the early and late

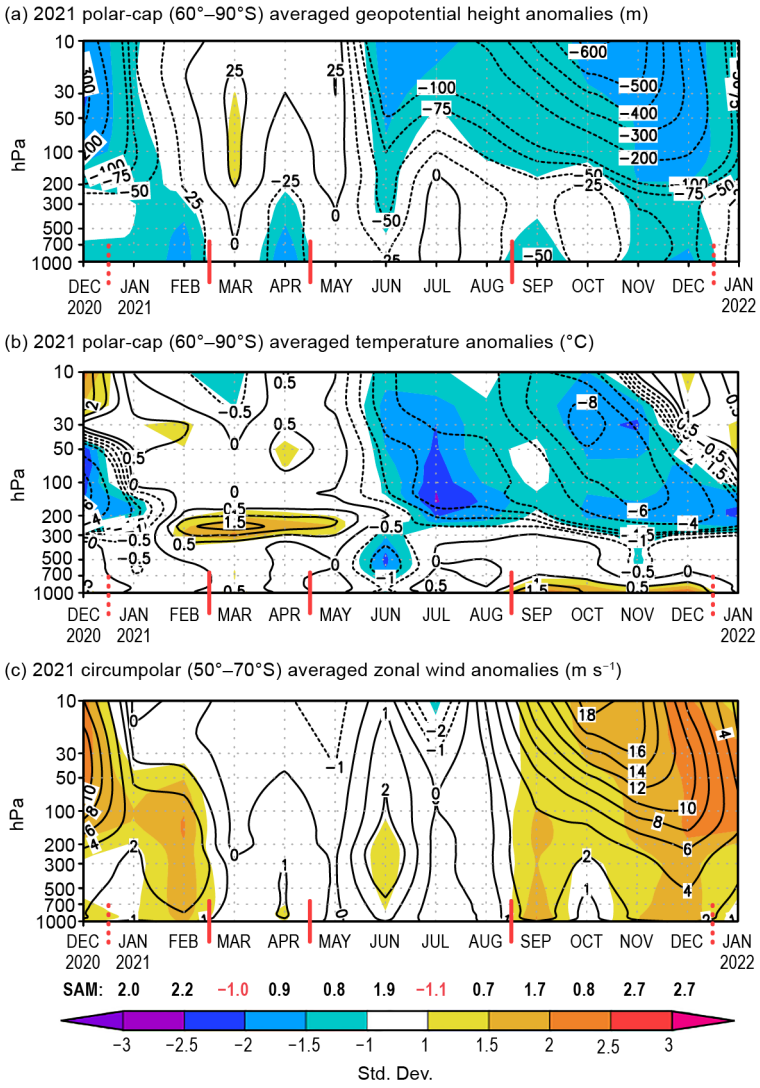

Fig. 6.2. Area-averaged (weighted by cosine of latitude) monthly anomalies over the southern polar region in 2021 relative to 1991–2020: (a) polar cap (60°–90°S) averaged geopotential height anomalies (contour interval is 25 m up to ±100 m and 100 m after ±100 m); (b) polar cap (60°–90°S) averaged temperature anomalies (contour interval is 0.5°C up to ±2°C and 2°C after ±2°C); (c) circumpolar (50°–70°S) averaged zonal wind anomalies (contour interval is 2 m s^{-1} with an additional contour at ±1 m s^{-1}). Shading depicts standard deviation of monthly anomalies from the 1991–2020 climatological average as indicated by the color bar at bottom. Red vertical bars indicate the four climate periods used for compositing in Fig. 6.3; the dashed lines near Dec 2020 and Dec 2021 indicate circulation anomalies wrapping around the calendar year. Values from the Marshall (2003) SAM index are shown below (c) in black (positive values) and red (negative values). (Source: ERA5 reanalysis.)

quarters, associated with the anomalously large and deep spring ozone holes in 2020 and 2021, respectively (Kramarova et al. 2021; see section 6h for more details). This resulted in near- or stronger-than-average circumpolar westerly winds for all of 2021.

The Antarctic atmospheric circulation anomalies were examined using the European Centre for Medium-Range Weather Forecasts fifth generation atmospheric reanalysis (ERA5). Figure 6.2 shows the monthly geopotential height (Fig. 6.2a) and temperature (Fig. 6.2b) anomalies averaged over the polar cap (60°–90°S) and the monthly circumpolar zonal wind anomalies (Fig. 6.2c) averaged over 50°–70°S. The anomalies (contoured) and the standard deviations (shaded) are relative to the 1991–2020 climatology. To highlight the main surface climate anomalies, the year was split into four periods based on relative persistence of climate anomalies: January–February, March–April, May–August, and September–December. The surface pressure and temperature anomalies (contours) and standard deviations (shaded) are averaged for each group relative to their 1991–2020 climatology (Fig. 6.3). Monthly temperature and pressure anomalies are also shown for select Antarctic staffed (Marambio, Neumayer, Davis) and automated (Relay Station AWS, Byrd AWS, Gill AWS) weather stations located throughout the continent (Fig. 6.4).

From January to February, strong negative geopotential height (Fig. 6.2a) and surface pressure (Fig. 6.3a) anomalies and below-average temperatures (Fig. 6.3b) dominated Antarctica. The negative pressure anomalies were accompanied by a ring of positive pressure anomalies across the middle latitudes, resulting in anomalously strong circumpolar westerlies through the troposphere and lower stratosphere (2–3 m s^{-1}, 1–2 std. dev. above average; Fig. 6.2c), reaching a peak in February. Neumayer station observed its coldest January on record, at −6.2°C (2.1°C below average; Fig. 6.4b), and just to the east, Novolazarevskaya station (not shown) observed its coldest February on record. While negative pressure anomalies occurred over the entire continent, they were strongest over West Antarctica where pressure was more than 10 hPa (3 std. dev.) below average (Fig. 6.3a); in this region, Byrd AWS and Gill AWS (on the Ross Ice Shelf) both observed their lowest mean February pressure on record, (10–11 hPa

below average; Figs. 6.4e,f), while on the plateau, Relay Station AWS also observed its lowest February pressure on record (6.7 hPa below average).

The negative pressure anomalies and cold temperatures over the continent relaxed during March–April (Figs. 6.3c,d), and a strong cyclonic anomaly developed across the Weddell Sea region. This brought marked surface warming across Dronning Maud Land and to parts of the plateau, which peaked during March when temperatures were 4–6°C (> 3 std. dev.) above average (not shown). Neumayer (Fig. 6.4b), Novolazarevskaya (not shown), and Relay Station AWS (Fig. 6.4d) all observed their warmest March on record. Neumayer also observed its lowest mean April pressure on record (Fig. 6.4b). In contrast, negative temperature anomalies were observed across Marie Byrd Land and the Ross Ice Shelf during March–April (Fig. 6.3d).

From May to August, surface pressure across the continent remained relatively stable and close to average, and a zonal wave-3 pattern developed over the Southern Ocean (Fig. 6.3e). The most noteworthy monthly feature occurred in June when negative surface pressure and geopotential height anomalies over the polar cap developed through the upper troposphere and lower stratosphere (Fig. 6.2a), coinciding with a strengthening of the circumpolar westerlies (Fig. 6.2c) and strong negative surface temperature anomalies near the pole (Fig. 6.3f). The South Pole recorded a June temperature of –63.9°C that was 5.8°C below average (see Sidebar 6.1) which equaled 1984 for its second coldest June temperature on record. No monthly temperature or pressure records were set over this period, but temperatures were 3–4°C (1–2 std. dev.) below average, stretching from the South Pole toward Dronning Maud Land, where Neumayer observed its coldest austral winter (June–August) on record (not shown), and the South Pole observed its coldest extended winter season (April–September, Sidebar 6.1) on record.

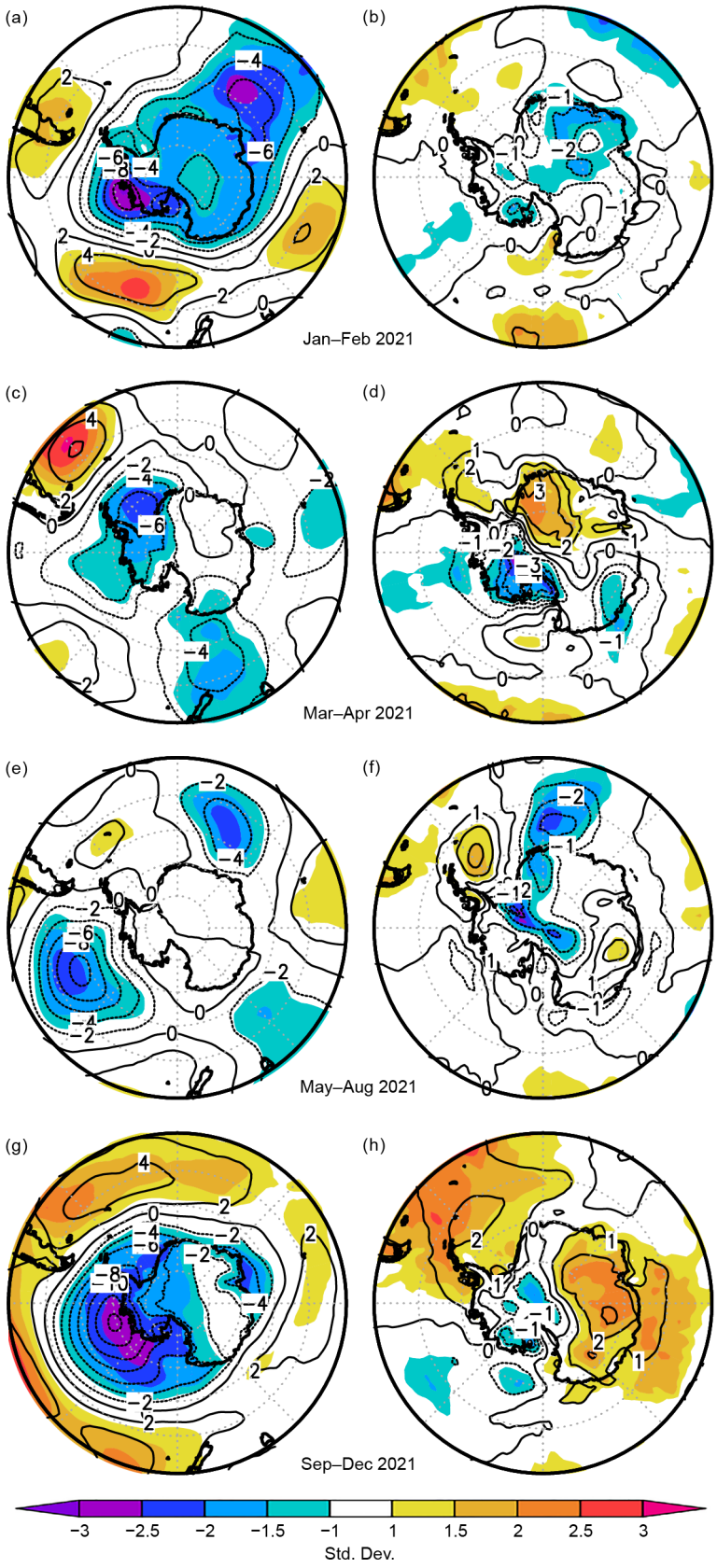

Fig. 6.3. (left) Surface pressure and (right) 2-m temperature anomalies relative to 1991–2020 for (a,b) Jan–Feb 2021; (c,d) Mar–Apr 2021; (e,f) May–Aug 2021; (g,h) Sep–Dec 2021. Contour interval is 2 hPa for surface pressure anomalies and 1°C for 2-m temperature anomalies. Shading shows the standard deviation of the anomalies. (Source: ERA5 reanalysis.)

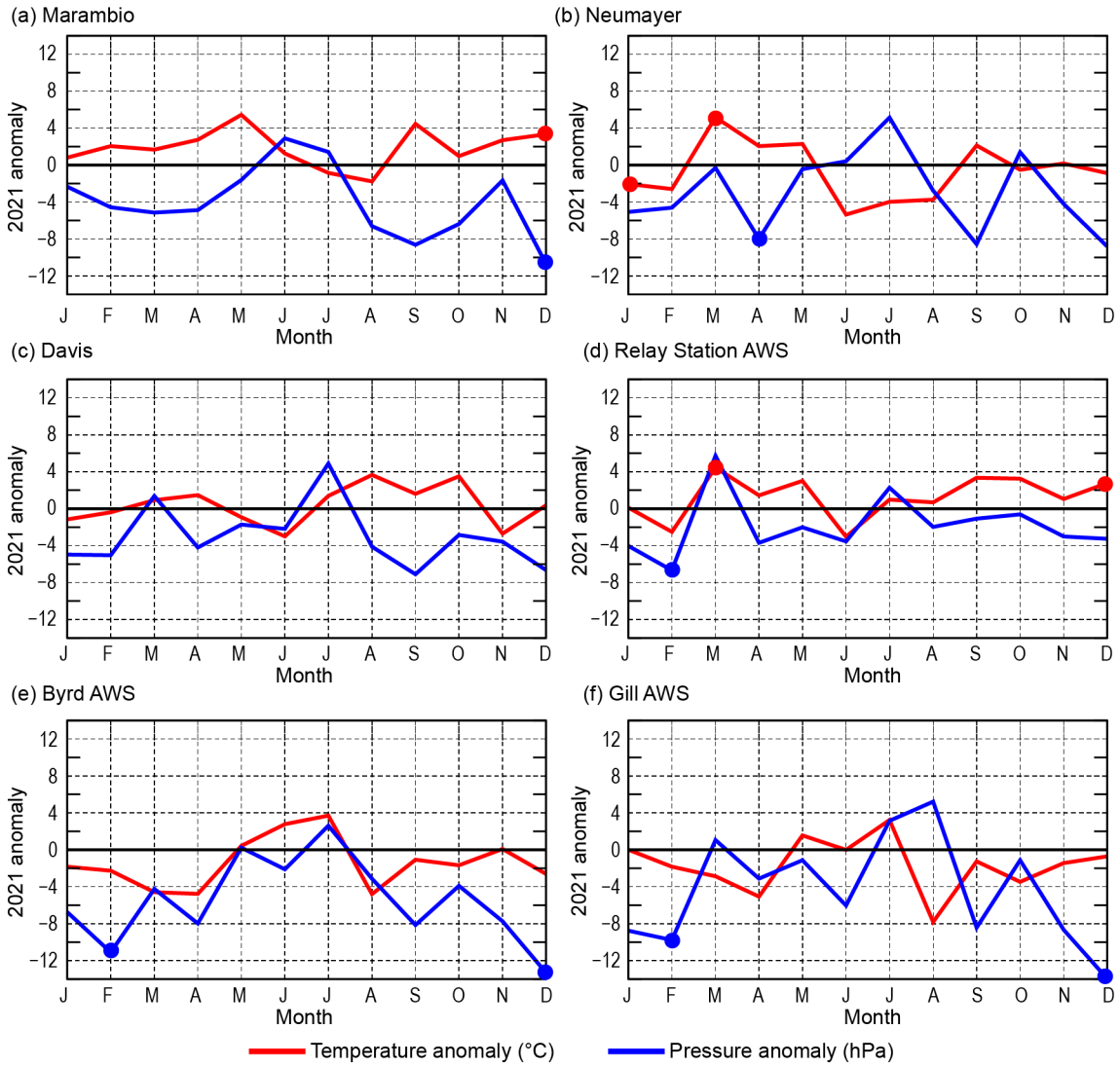

Fig. 6.4. Monthly Antarctic climate anomalies during 2021 at six representative stations (three staffed [a–c], and three automatic [d–f]). Anomalies for temperature (°C) are shown in red and MSLP/surface pressure (hPa) are shown in blue, with filled circles denoting monthly-mean records set for each station in 2021. All anomalies are based on differences from the monthly 1991–2020 averages. Observational data used to calculate records start in 1970 for Marambio, 1981 for Neumayer, 1957 for Davis, 1980 for Byrd AWS, 1995 for Relay Station AWS, and 1985 for Gill AWS.

Surface pressure was below average again in most regions from September to December, especially across West Antarctica and over the Amundsen Sea (Fig. 6.3g). Negative pressure anomalies along coastal West Antarctica of –12 to –14 hPa (> 2.5 std. dev.) were associated with warm air advection across the Antarctic Peninsula and Weddell Sea region and temperatures were 1–2°C (> 2 std. dev.) above average (Fig. 6.3h). Austral spring (September–November) was especially warm on the Peninsula, with Faraday, Rothera, Bellingshausen, and Esperanza all experiencing one of their three warmest springs on record (not shown). Meanwhile, in early spring East Antarctica also experienced temperatures that were 2–3°C (2 std. dev.) above average over this period on the plateau (Fig. 6.3h) and 3–4°C above average at the coast near Davis (Fig. 6.4c). Strong negative pressure anomalies were observed over the continent in November and December, with Marambio, Byrd AWS, and Gill AWS all setting new low-pressure records in December, while Marambio and Relay AWS both tied for their warmest Decembers on record. These large Antarctic climate anomalies in late 2021 were likely a result of the downward propagation of negative geopotential height anomalies from the stratosphere to the lower troposphere (Fig. 6.2a) via dynamical and diabatic forcing (Song and Robinson 2004; Thompson et al. 2006) from the anomalously deep ozone hole and associated stratospheric anomalies in 2021 (section 6h).

Sidebar 6.1: A record cold winter at the South Pole in 2021—T. NORTON, L. KELLER, K. R. CLEM, M. LAZZARA, T. SCAMBOS, AND S. BARREIRA.

The Amundsen-Scott South Pole station had its lowest austral winter average temperature in 2021, at –61.0°C (April–September, AMJJAS; blue line in Fig. SB6.1a) since records began in 1957. During these months when the South Pole is in continuous darkness, there were 153 days (out of 183) where the daily average temperature was –50°C or below, second only to the polar night period in 2012. Meteorological winter (June–August, JJA) was the second coldest on record (behind 2004), with June and August each having 28 days at or below –50°C. The annual mean temperature for the 2021 calendar year tied for third coldest on record at –50.5°C (red line in Fig. SB6.1a), 1.3°C below average.

Generally, a stable polar vortex creates prime conditions for extensive cold periods by minimizing the intrusions of warm air into the continental (ice sheet) interior. Clear sky conditions augment the tendency towards low temperatures by increasing radiative cooling, and low wind speeds reduce mixing of boundary layer air, resulting in a strong surface inversion (Neff et al. 2018; Keller et al. 2022). Under strong inversion conditions, the mean wind direction at the South Pole is grid east/northeast (40°–80°; Neff et al. 2018; Keller et al. 2022), as air drains off the East Antarctic Plateau. All of these factors were in play in 2021, resulting in a polar night that was substantially colder than average, although records were not set in any of the individual months. Further, the below-average annual mean temperature in 2021 did not substantially reduce the overall warming trend over the last 30+ years at the South Pole (Clem et al. 2020). The annual mean temperature trend from 1989 to the record warm year in 2018 is 0.61 ± 0.34°C decade^{-1} ($p < 0.01$, solid black line in Fig. SB6.1a), and it remains positive (although smaller) and significant when the trend is extended to 2021 at 0.47 ± 0.32°C decade^{-1} ($p < 0.01$; dashed black line in Fig. SB6.1a).

The persistent cold from April to September 2021 was a result of multiple compounding factors. Although the Amundsen Sea Low (ASL) was anomalously strong during AMJJAS, shown by the large negative geopotential height anomalies (contours) in Fig. SB6.1b, the center of the cyclonic anomaly in 2021 was located in the southernmost South Pacific near 60°S, north of its winter average position of ~70°S (Hosking et al. 2013) and away from the continent. This limited the advection of warmer, maritime air to the Antarctic Peninsula and West Antarctic coastline. By comparison, the anomalous cyclonic circulation in 2018 extended eastward and poleward into the Weddell Sea and across West Antarctica, driving warm air inland. In addition, a large cyclonic anomaly dominated winter conditions in Dronning Maud Land in 2021 compared to a strong anticyclone in 2018. This extended onto the East Antarctic Plateau, producing anomalous easterly flow off the high Polar Plateau clockwise towards the Weddell Sea, suppressing the intrusion of warm air masses off the Weddell Sea, unlike what occurred in 2018.

Comparing the 2021 synoptic conditions (blue lines in Figs. SB6.1c–f) with those of 2018 (red lines), the South Pole's anomalous warm conditions in 2018 peaked during May–August (Fig. SB6.1c), coinciding with a higher-than-average number of cloudy days (Fig. SB6.1d), which would reduce radiative cooling. In 2021, July and August had significantly clearer sky conditions, which in conjunction with the cold air flow off the plateau (Fig. SB6.1b), would further amplify the cold conditions. Satellite composite imagery (https://doi.org/10.48567/hevb-j127) confirmed the persistent clear skies over the South Pole and the limited maritime air mass intrusions through the winter. Cloud movement patterns indicated that continental air was trapped over the interior for extended periods, with little low-latitude air intrusion. The monthly average vector wind directions observed at the South Pole between June and September were between 50° and 80° (grid northeast/east; not shown), which were 10°–30° east of average (Fig. SB6.1e), consistent with cold air advection from the higher plateau. This contrasts with the anomalous westerly wind directions in 2018 that are more consistent with onshore flow from the Weddell Sea. Monthly average vector wind speeds were also anomalously low, particularly in the last three quarters of the year (Fig. SB6.1f). In comparison, 2018 saw above-average wind speeds, particularly during May and June when the largest positive temperature anomalies occurred. The combination of colder, easterly flow from the plateau, radiational cooling, and reduced mixing due to anomalously low wind speeds all contributed to the comparatively cold 2021 winter (Keller et al. 2022).

From this analysis, it is evident that small changes in local conditions can result in large temperature anomalies at the South Pole, which could help to explain why interannual variability in temperature at the South Pole is substantial (Clem et al. 2020). While there is uncertainty in the precise role of each mechanism given the unique atmospheric environment at the South Pole during the winter, regional and local wind direction, wind speed, and cloud cover all appear to be important and contribute to the large interannual variability, especially when contrasting the conditions with 2018.

While the difference in mean winter temperature between 2021 and recent years is dramatic, the underlying conditions that

favor warming at the South Pole may still be at play (Clem et al. 2020; Stammerjohn and Scambos 2020) and the significant long-term warming trend remains. However, the 2021 winter underscores the high degree of interannual variability seen in the southern continent and surrounding ocean, a quality that is reflected in sea ice conditions, accumulation patterns, and oceanic characteristics.

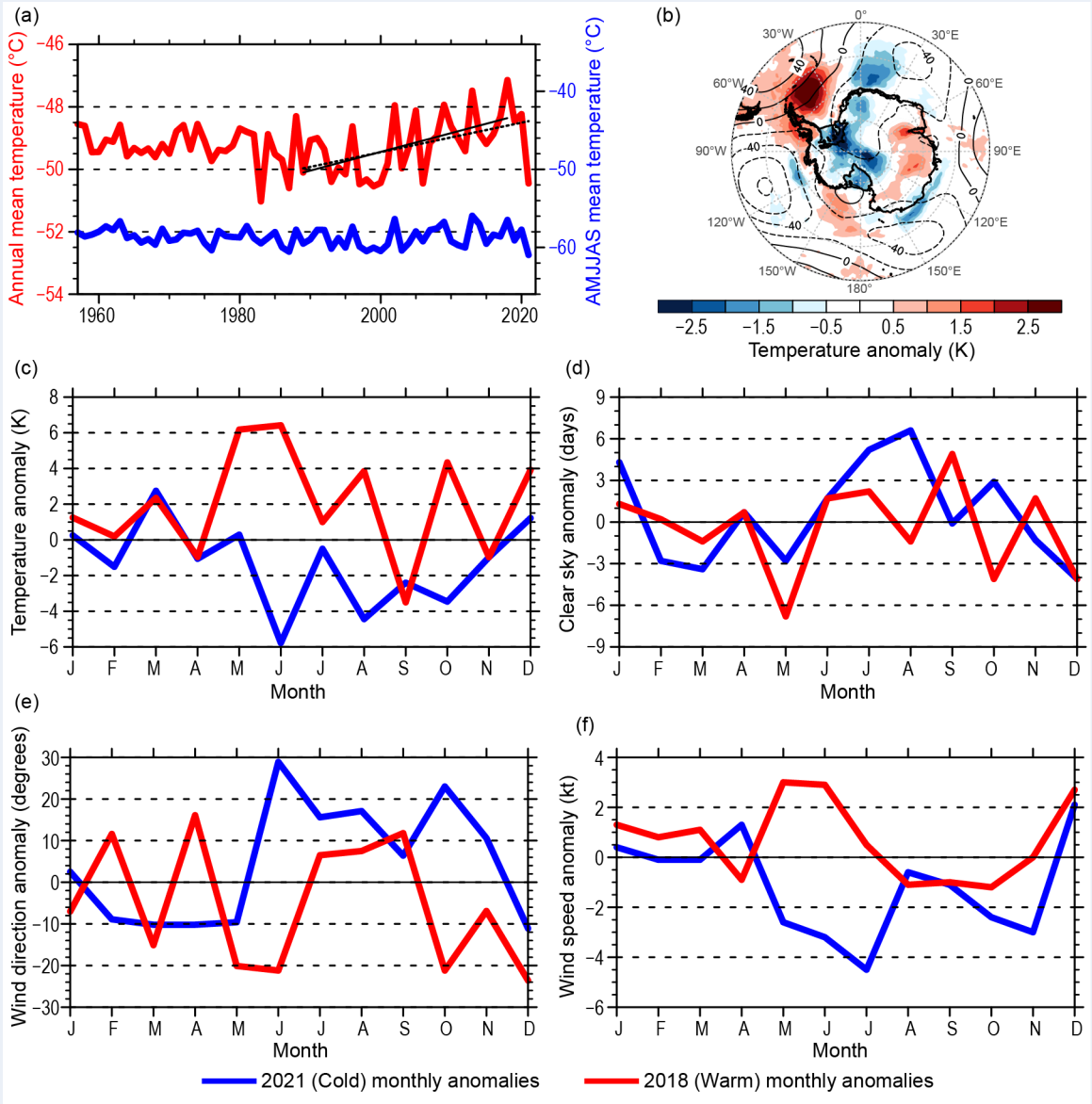

Fig. SB6.1. (a) Observed annual mean (red line) and Apr–Sep, AMJJAS, mean (blue line) South Pole temperature during the period 1957–2021. Also shown are the linear trend lines for 1989–2018 (solid black line) and 1989–2021 (dashed black line). (b) The 2021 AMJJAS 500-hPa geopotential height (m) and 2-m temperature (K) anomalies relative to the 1991–2020 climatology. (Source: ERA5.) (c)–(f) The observed 2021 (blue lines) and 2018 (red lines) monthly anomalies in (c) temperature, (d) number of clear sky days, (e) wind direction, and (f) wind speed at the South Pole relative to the 1991–2020 monthly climatologies.

c. Ice sheet surface mass balance—R. T. Datta, D. Dunmire, B. Baiman, M. Maclennan, and J. Wille

Surface mass balance (SMB) is the net effect of all processes that add to (precipitation) or take away (sublimation/runoff) mass from the surface of the ice sheet. Because the Antarctic Ice Sheet (AIS) is characterized by a cold climate, only in peak summer are atmospheric temperatures high enough to produce widespread surface melt or liquid precipitation anywhere on the grounded ice sheet (section 6d). Any meltwater that is produced refreezes locally in the firn (dense recrystallized snow left over from previous seasons), implying that meltwater runoff is generally negligible

on the AIS. On the other hand, sublimation is a significant contributor to AIS SMB (Agosta et al. 2019; Lenaerts and Van Den Broeke 2012; Mottram et al. 2020), especially in summer and in the windy escarpment zones of the ice sheet, where blowing snow occurs frequently (> 50%, Palm et al. 2018). The dominant contributor of AIS SMB, with an approximate magnitude of ~2300 Gt yr^{-1} (from reanalysis) over the grounded AIS, is solid precipitation (snowfall). In both absolute terms and as a driver of interannual variability, precipitation is strongly affected by sporadic extreme events, often in the form of atmospheric rivers (ARs; Turner et al. 2019; Wille et al. 2021). Future SMB trends indicate a divergence in SMB behavior as temperatures increase, with ice shelves being strongly affected by melt while the grounded ice sheet receives enhanced precipitation (Kittel et al. 2021).

Atmospheric reanalysis products are useful tools to analyze AIS SMB and its two dominant contributors, snowfall and sublimation, in near-real time. Here we use MERRA-2 (0.5° × 0.625° horizontal resolution; Gelaro et al. 2017) and ERA5 (0.25° × 0.25° horizontal resolution) to analyze the 2021 AIS SMB, its spatial and seasonal characteristics, and compare it to its climatological (1991–2020) record. Based on recent work comparing reanalysis products with in situ observations on Antarctica, MERRA-2 and ERA5 stood out as best-performing; however, important biases remain, including an overestimation of near-surface temperatures over the AIS interior during winter (Gossart et al. 2019; Medley and Thomas 2019; Wang et al. 2016).

The climatological AIS SMB from MERRA-2 and ERA5 is 2155 ± 128 Gt yr^{-1} and 1977 ± 103 Gt yr^{-1}, respectively. While the AIS SMB from ERA5 is significantly ($p < 0.05$) drier than MERRA-2, both reanalyses have comparable interannual variations during the climatological period and neither suggest a significant long-term trend in SMB (not shown). The 2021 AIS SMB was 2277 Gt according to MERRA-2, which falls within 1 standard deviation (std. dev.) of the climatological mean, and 2118 Gt according to ERA5, which is more than 1 std. dev. above the climatological mean for that dataset. Since both reanalyses produce similar spatial results, we use MERRA-2 hereafter to focus on spatial characteristics of the 2021 SMB. As described by various studies, AIS SMB (also in 2021, Fig. 6.5a) is relatively high (> 500 mm water equivalent) in the coastal areas of the ice sheet and decreases sharply from the coast upward and poleward on the ice sheet, with SMB values < 50 mm water equivalent (w.e.) in the high-elevation interior of the East Antarctic Ice Sheet.

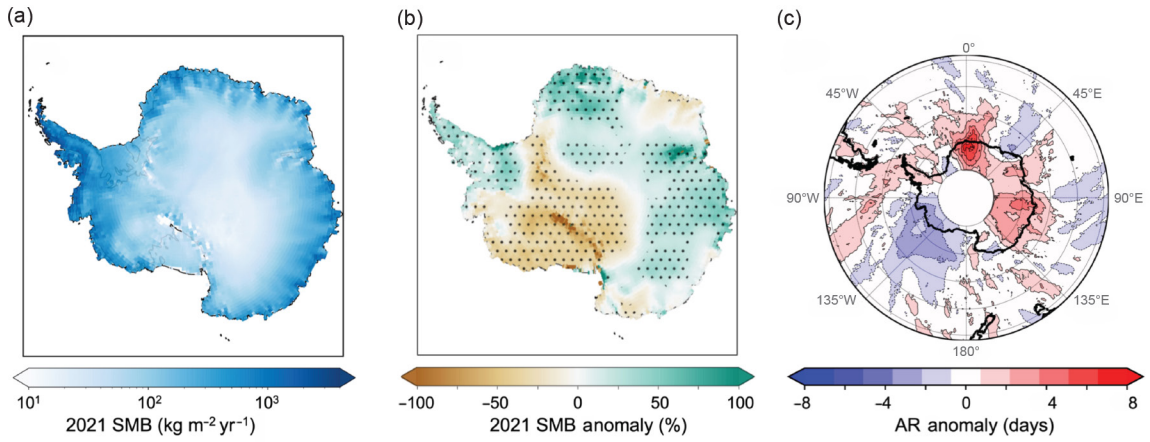

Fig. 6.5. (a) 2021 SMB in (kg m^{-2} yr^{-1}). (b) 2021 SMB anomaly(%) relative to 1991–2020 mean. 2021 SMB anomaly is greater than the 1991–2020 standard deviation in the stippled areas. (c) 2021 atmospheric river (AR) occurrence anomaly in number of days relative to the 1991–2020 mean.

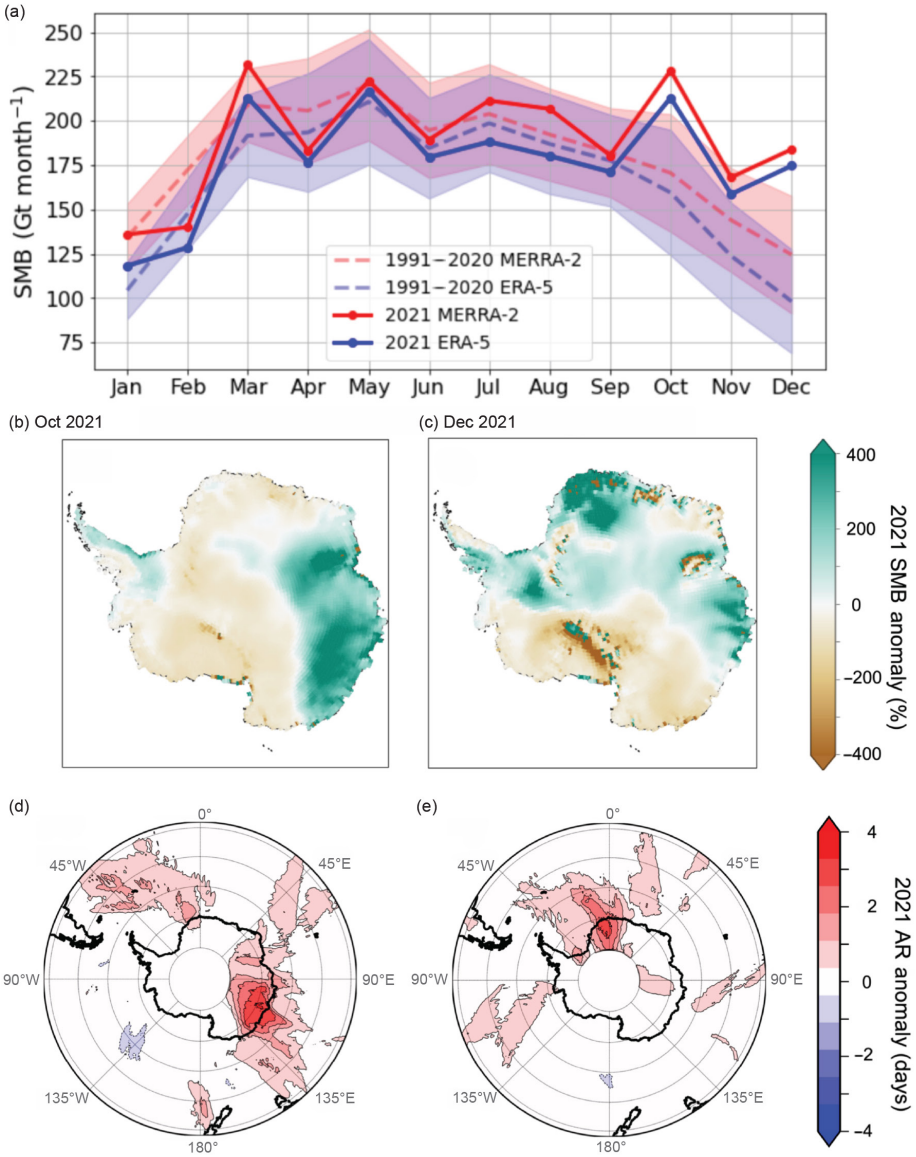

Fig. 6.6. (a) Seasonal cycle of (grounded) Antarctic Ice Sheet integrated surface mass balance in Gt yr^{-1}, according to MERRA-2 (red) and ERA5 (blue), with 2021 values shown in solid lines, 1991–2020 mean shown in the dashed lines with shading indicating one standard deviation. MERRA-2 SMB anomaly for the month relative to the 1991–2020 mean for (b) Oct 2021 and (c) Dec 2021. Anomalous number of days when an atmospheric river (AR) was detected for the month compared to the 1991–2020 mean for (d) Oct 2021 and (e) Dec 2021.

SMB anomalies in 2021 from MERRA-2 indicate substantial spatial variability relative to the climatology (Fig. 6.5b). In particular, SMB was significantly lower than climatology (< 50% of the climatological mean) over Marie Byrd Land (135°W longitude), suggesting that low SMB in this region will supplement the dynamic mass loss again in 2021, which has been ongoing in the region (section 6e). Conversely, 2021 SMB was exceptionally above average in western Dronning Maud Land and Wilkes Land (> 150% of the climatological mean) and slightly higher over the Antarctic Peninsula (> 125% of the climatological mean). The SMB anomalies in these regions are mirrored by AR anomalies over the year (Figs. 6.5c, 6.6d,e), calculated using the algorithm originally presented by Wille et al. (2021) calculated from the 98th percentile of meridional integrated vapor transport over the time series, shown here in anomalous numbers of days where ARs occurred. These results emphasize the importance of high-impact AR occurrences to total SMB and in controlling regional interannual snowfall variability.

Throughout the year, the climatological AIS SMB varies considerably (Fig. 6.6), with a minimum in summer (120–140 Gt month^{-1}) and a maximum in autumn and spring (220–240 Gt month^{-1}). In 2021, the seasonal cycle for SMB diverged substantially from climatology in October and December, concurrent

with anomalously low pressure and above-average temperatures over the continent (section 6b). In these months, SMB values exceeded the monthly climatological mean by 1 std. dev. for MERRA-2 (shown in red shading) as well as in ERA5 (shown in blue shading). SMB anomaly maps indicate that these months in 2021 were characterized by strong anomalies in Wilkes Land (October, Fig. 6.6b) and in Dronning Maud Land (December, Fig. 6.6c), driven by frequent AR activity over these regions (Figs. 6.6d,e, respectively). These periods were also characterized by positive SMB anomalies over the eastern AP (October, Fig. 6.6b) and over the western AP (December, Fig. 6.6c), despite a lack of anomalous AR activity in the region.

d. Ice sheet seasonal melt extent and duration—M. MacFerrin, T. Mote, A. Banwell, and T. Scambos

Surface melt on the Antarctic Ice Sheet (AIS) occurs primarily on the coastal margins, especially on the Antarctic Peninsula and Antarctica's ice shelves. It is generally not a significant component of Antarctica's net surface mass balance because few areas have significant runoff of meltwater. However, surface melt has a large effect on the density of underlying glacial firn and can induce calving and/or glacier acceleration through hydrofracture (Scambos et al. 2003; Banwell et. al. 2013) and is important to monitor for ice sheet and ice shelf stability. The austral melt season is defined here as 1 October through 30 April. Although small brief melt events can be measured along Antarctica's northern coastal margins during austral winter, the vast majority of surface melt happens during these seven months, with the most melt being typically in December and January (Johnson et al. 2021). Here we focus on the 2020/21 melt season ending 30 April 2021. The 2021/22 austral melt season will be discussed in next year's report.

Daily surface melt is mapped using satellite passive-microwave brightness temperatures. The source data are distributed as daily composited polar stereographic brightness temperatures by the National Snow and Ice Data Center (products NSIDC-0001; Meier et al. 2019 and NSIDC-0007; Gloersen 2006) spanning 1979 through present-day. Daily passive microwave brightness temperatures using the 37-GHz horizontal polarization as well as the 37- and 19-GHz vertical polarization channels are acquired by the SMMR, SSM/I, and SSMIS sensors aboard the NOAA Nimbus-7 and DMSP F8, F11, F13, F17, and F18 satellites. Melt is determined by 37-GHz horizontally polarized brightness temperatures that exceed a dynamically established threshold each season from a simple microwave emission model that would be expected in the presence of liquid water in near-surface layers of ice and snowpack. The method used here was first developed to track Greenland's ice sheet surface melting on a daily basis (Mote and Anderson 1995; Mote 2007; Mote et al. 2014). Melt days are mapped both as sums over the melt season and as anomalies with respect to the mean annual melt day totals from the 1990–2020 baseline melt period (Figs. 6.7a,b). Large seasonal fluctuations in passive microwave emissions from some areas of dry polar firn in Antarctica can create false positive melt indications in an unmodified version of the Greenland algorithm. This was mitigated by filtering areas that only marginally exceed the melt threshold (< 10K) in the 37 GHz horizontal polarization in regions with a negative 18/19-GHz minus 37-GHz frequency gradient in the vertical polarization (MacFerrin et al. 2021). An ice extent mask of 25-km grid cells for the AIS was developed from the Quantarctica v3.0 Detailed Basemap dataset (Norwegian Polar Institute 2018). All 25-km cells that contain ≥ 50% land-ice or ice-shelf are included. We divide the AIS into seven melt extent and climate regions by clustering glaciological drainage basins (based on Shepherd et al. 2012; Fig. 6.8).

The 2020/21 austral melt season began early, with a spatially and temporally extensive melt event on the Antarctic Peninsula in the last days of October into early November (Fig. 6.7c). On the Peninsula, over the northern Larsen C and Larsen B remnant ice shelves in the 2020/21 season, there were approximately 30 more melt days than during the 1990–2020 reference period (Figs. 6.7a, 6.8b). The mid-peninsula regions, including the George VI Ice Shelf and the Wilkins Ice Shelf, had near-average to below-average melt seasons in duration and extent, particularly in comparison to the exceptional melt season that occurred on these ice shelves during the 2019/20 austral melt season (Banwell et al. 2021; MacFerrin et al. 2021). By contrast, the southern area

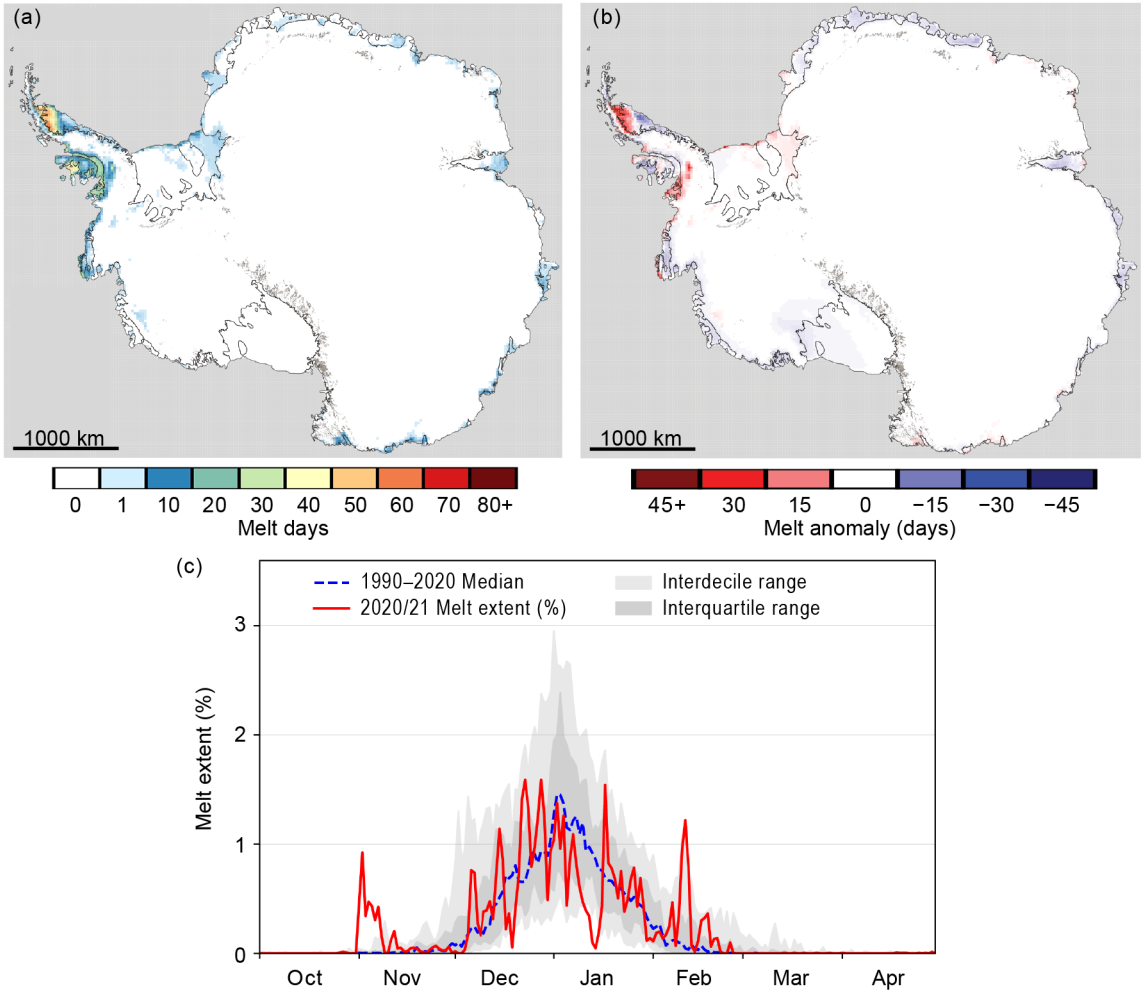

Fig. 6.7. Surface melt across the Antarctic Ice Sheet as detected from passive-microwave satellites. (a) Map of the sum of melt days from 1 Oct 2020 to 30 Apr 2021. (b) Map of the sum of melt days relative to the 1990–2020 baseline average. (c) Daily melt extent (dotted blue line) with interquartile (dark gray) and inter-decile (light gray) ranges from the 1990–2020 baseline period.

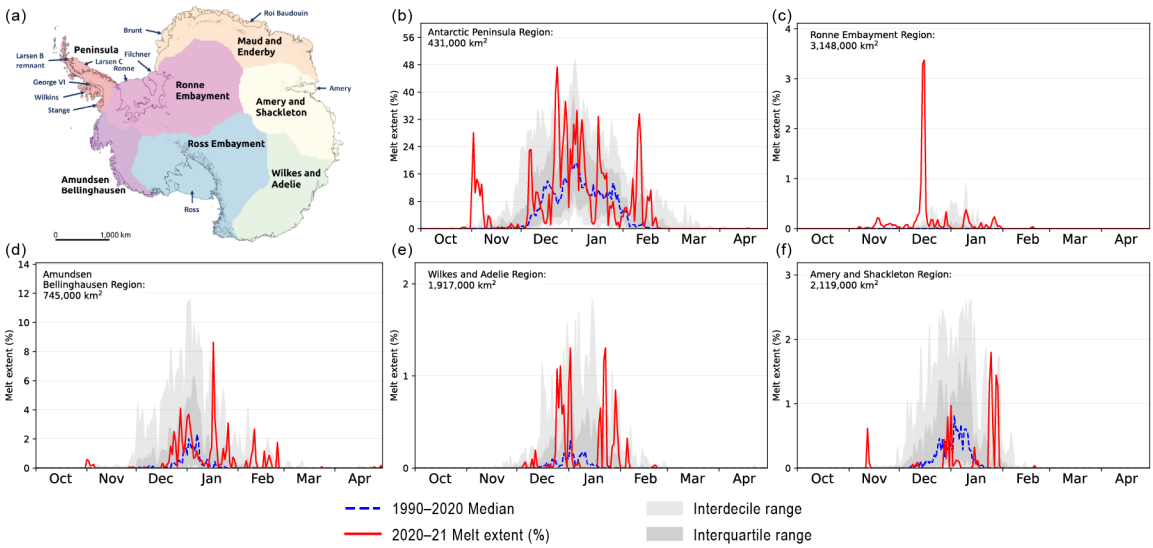

Fig. 6.8. Daily melt extents across regions of Antarctica. (a) Map of major regions of Antarctica used in regional analyses. Regional daily melt extents from (b) the Antarctic Peninsula, (c) Ronne Embayment, (d) Amundsen Bellingshausen, (e) Wilkes and Adelie, and (f) Amery and Shackleton.

of the Peninsula had an above-average number of melt days, notably in the area of the Stange Ice Shelf. Elsewhere, it is the absence of melt that is most notable: the Amery Ice Shelf (Fig. 6.8f) had 5 to 10 days of below-average melt days with only two notable melt events occurring in late January; the Roi Baudoin Ice Shelf had about 10 melt days below average overall; and on the northeastern Ross Ice Shelf, essentially zero surface melt was recorded for the season. Total melt for the season over the continent was moderately above average (Fig. 6.7a). The Peninsula, Ronne Embayment, Wilkes and Adelie, and Amundsen-Bellingshausen regions showed above-average melt indices, while the Maud and Enderby, Amery and Shackleton, and Ross Embayment regions displayed below-average melt.

On the Filchner and Brunt ice shelves, a brief but extensive melt event occurred in mid-December that reached far to the south, covering the entire length of the Filchner shelf on the eastern edge of the Ronne Ice Shelf (Figs. 6.7a, 6.8c). High atmospheric pressure in Queen Maud Land and a large low-pressure area stretching across the Ronne Ice Shelf drove strong winds from the north, bringing warm conditions all along Coats Land and as far south as the South Pole (section 6b). The South Pole remained well below freezing, but temperatures were still above average during this period. Such anomalous incursions of warm air in this region are consistent with changes in atmospheric circulation that have favored relative warm air incursions in the Ronne Embayment region deep into the continent (Stammerjohn and Scambos 2020; Clem et al. 2019, 2020), with relatively decreasing amounts of melt occurring on the Peninsula compared to the early 2000s (Barrand et al. 2013; Olivia et al. 2017). It remains unclear if this change in circulation patterns is part of a long-term trend or natural variability (Turner et al. 2016).

e. Ice sheet mass balance—S. Adusumilli, H. A. Fricker, and A. S. Gardner

The Antarctic Ice Sheet (AIS) gains mass from accumulation (snowfall minus sublimation) at the surface and primarily loses mass at the margins through its floating extensions, called ice shelves. Mass loss can occur due to the episodic calving of icebergs at ice shelf fronts, which occurs at multi-annual to multi-decadal time scales, or through continuous ocean-driven basal melting under ice shelves (Rignot et al. 2013; Depoorter et al. 2013; Adusumilli et al. 2020). For any given time period, the net mass balance between competing mass gains and losses depends on interactions between the ice, ocean, and atmosphere (e.g., Smith et al. 2020a). Over the past two decades, the ice sheet has experienced net mass loss of grounded ice (e.g., The IMBIE Team 2018), which is in part due to net mass loss of its floating ice shelves (e.g., Paolo et al. 2015) and a corresponding reduction in their "buttressing" effect that otherwise slows the flow of grounded ice into the ocean (e.g., Gudmundsson et al. 2019). Mass loss over the ice sheet has sometimes occurred rapidly in the past (e.g., during the collapse of Larsen B Ice Shelf; Scambos et al. 2004), stressing the need for continuous monitoring through satellite observations.

Since 2018, data from the ICESat-2 mission have been used to show elevation changes in the ice sheet at higher spatial and temporal resolution compared to earlier observations and have provided important information on the processes occurring at these scales. Several studies published during 2020–22 have used ICESat-2 data to provide new observations of the ice sheet, advancing our understanding of surface melt and drainage (Warner et al. 2021); supraglacial lake volumes (Fair et al. 2020; Fricker et al. 2020; Datta et al. 2021); the movement of subglacial water below the ice sheet (Neckel et al. 2021; Siegfried and Fricker 2021); dynamics at grounding zones zones (Li et al. 2022); biases between radar- and laser-derived estimates of height (Aublanc et al. 2021); the ongoing weakening of Thwaites Eastern Ice Shelf (Alley et al. 2021; Wild et al. 2022); the calving of the large tabular icebergs (Walker et al. 2021); and the calving of small icebergs through buoyancy-driven flexure at the ice shelf front (Becker et al. 2021).

At the time of writing, there were no published estimates of total Antarctic mass or height change for 2021. Therefore, we derive estimates of height changes over the ice sheet from NASA's ICESat-2 laser altimeter for the latest annual data available: November 2020 to November 2021. We used the

ATLAS/ICESat-2 ATL06 L3A Land Ice Height, Version 5 data product (Smith et al. 2020b), which provides precise estimates of height along repeated ground tracks. We derived along-track height changes between Cycle 9 (October–December 2020) and Cycle 13 (October–December 2021) from these data (Fig. 6.9a). We smoothed the final height change map using a Gaussian filter with a 30-km diameter. The conversion of height changes to mass changes requires a firn density model (e.g., Ligtenberg et al. 2011), which is not yet available for this period. We do not derive results for the ice shelves for 2021.

We also show annual mass anomalies derived from NASA's satellite gravimeter (GRACE-FO; Fig. 6.9b). We used data from the JPL GRACE and GRACE-FO Ocean, Ice, and Hydrology Equivalent Water Height Coastal Resolution Improvement (CRI) Filtered Release 06 Version 02 mascon data that solve for mass anomalies on 300-km diameter spherical caps (Wiese et al. 2022). We calculated gravity-derived mass anomalies for the same November 2020 to November 2021 period as used for ICESat-2, with the same 3-month averaging. To determine ice sheet mass anomalies, we identified all mascons containing more than 10,000 km^2 of land, according to the provided Coastline Resolution Improvement (CRI) land mask. We interpolated the area-averaged rates of change using bilinear interpolation according to the location of the geometric center of the land area contained within the mascon. We then masked all non-land areas using the Bedmachine ice mask (Morlighem et al. 2020).

The maps of annual changes in ice sheet height from ICESat-2 (Fig. 6.9a) and mass from GRACE-FO (Fig. 6.9b) show ongoing losses of ice in the Amundsen Sea sector of West Antarctica, the same region where losses have been observed over the previous decade (Smith et al. 2020a). There was a net mass loss over the ice sheet between December 2020 and December 2021 of 50 Gt (not shown), much lower than the average annual mass loss of 140 Gt yr^{-1} between December 2003 and December 2021. This lower-than-average mass loss was likely due to surface mass gains across the Antarctic Peninsula, Dronning Maud Land, and Wilkes Land associated with an above-average number of landfalling atmospheric rivers in those regions (section 6c), which partially offset (but did not fully compensate for) the large mass losses in West Antarctica.

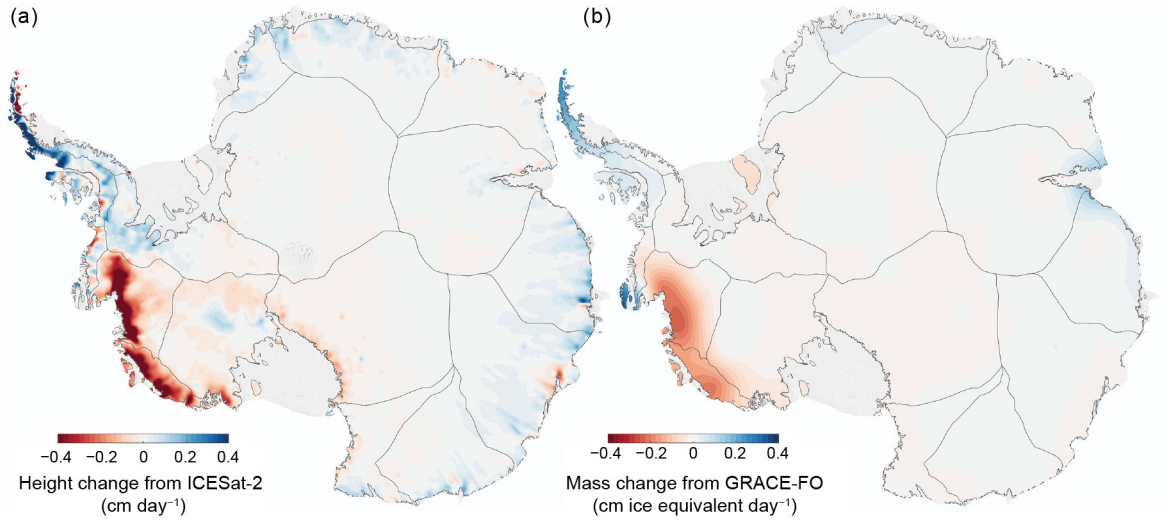

Fig. 6.9. Maps of (a) height change (cm day^{-1}) from ICESat-2 and (b) ice equivalent mass change (cm ice equivalent day^{-1}) from GRACE-FO for the period Nov 2020 to Nov 2021.

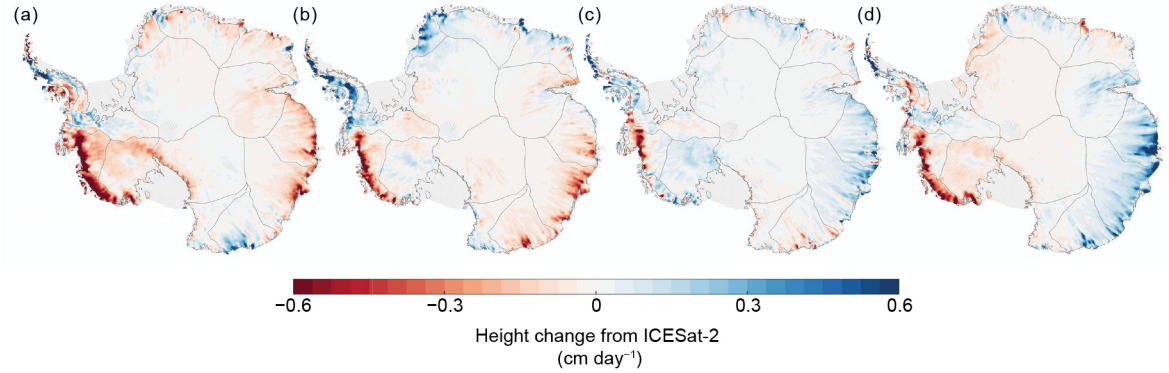

Fig. 6.10. Maps of height change (cm day^{-1}) from ICESat-2 for (a) Nov 2020–Feb 2021, (b) Feb–May 2021, (c) May–Aug 2021, and (d) Aug–Nov 2021. Dates represent the central month of each 3-month ICESat-2 data acquisition cycle.

To examine seasonal variability, we also derived height changes from ICESat-2 at 3-month intervals between November 2020 and November 2021 period using the technique described above for deriving the annual height change map (Fig. 6.10). Although data from the GRACE-FO mission were available at monthly intervals during this period, a small seasonal bias in the AIS mass change signal has been noticed in the GRACE-FO data, which is due to the accelerometer transplant calibration (the accelerometer on one spacecraft is currently not used due to noise; Harvey et al. 2022). This bias is related to the orbital beta-angle, and thus affects the seasonal variations only. The mission's Science Data System has developed an updated accelerometer calibration that removes this seasonal bias in the next data release (planned for boreal spring 2022; F. Landerer, person. comm.). Therefore, we only include annual estimates of ice sheet mass loss from GRACE-FO in this report. Many of the spatial patterns of increases in height across Antarctica correspond well with patterns of positive surface mass balance anomalies reported in 2020 (see Fig. 6.5b). For example, large increases in height over Wilkes Land, East Antarctica, during August–November (Fig. 6.10d) coincided with increases in the frequency of landfalling atmospheric rivers (Adusumilli et al. 2021) during this period (see Fig. 6.6d). This further suggests a major contribution of surface processes in driving seasonal height and mass changes. Meanwhile, decreases in height continued to dominate coastal West Antarctica for all of 2021.

f. Sea ice extent, concentration, and seasonality—P. Reid, S. Stammerjohn, R. A. Massom, S. Barreira, T. Scambos, and J. L. Lieser

During 2021, and following on from 2020, net Antarctic sea ice coverage continued to exhibit strong variability (Fig. 6.11a), with distinct regional and seasonal contributions (Fig. 6.11b). The year began with below-average overall sea ice extent (SIE) in January through February (Fig. 6.11a), compared to the 1991–2020 average, but abruptly switched to above average in late February where it remained almost continuously until early September. Sea ice then retreated at rates faster than average, with net SIE at ~1.5 × 10^6 km^2 below average in late December. Annual daily minimum SIE occurred on 22 February (2.68 × 10^6 km^2), which was slightly below average, while the annual daily maximum (18.79 × 10^6 km^2) was slightly above average but very early (30 August)—the second earliest daily maximum on record. Sea ice area (SIA), which is the product of SIE and concentration, followed a similar overall pattern to SIE but attained near record-high levels in late August (second highest on record), before plummeting to record-low daily values during parts of October and December. A new monthly-mean low SIA (5.45 × 10^6 km^2) was recorded for December. In terms of regional contributions, the western Weddell, Bellingshausen, and Ross Seas sectors generally experienced smaller-than-average SIE through much of 2021, whereas the Amundsen Sea sector recorded larger-than-average SIE through the year.

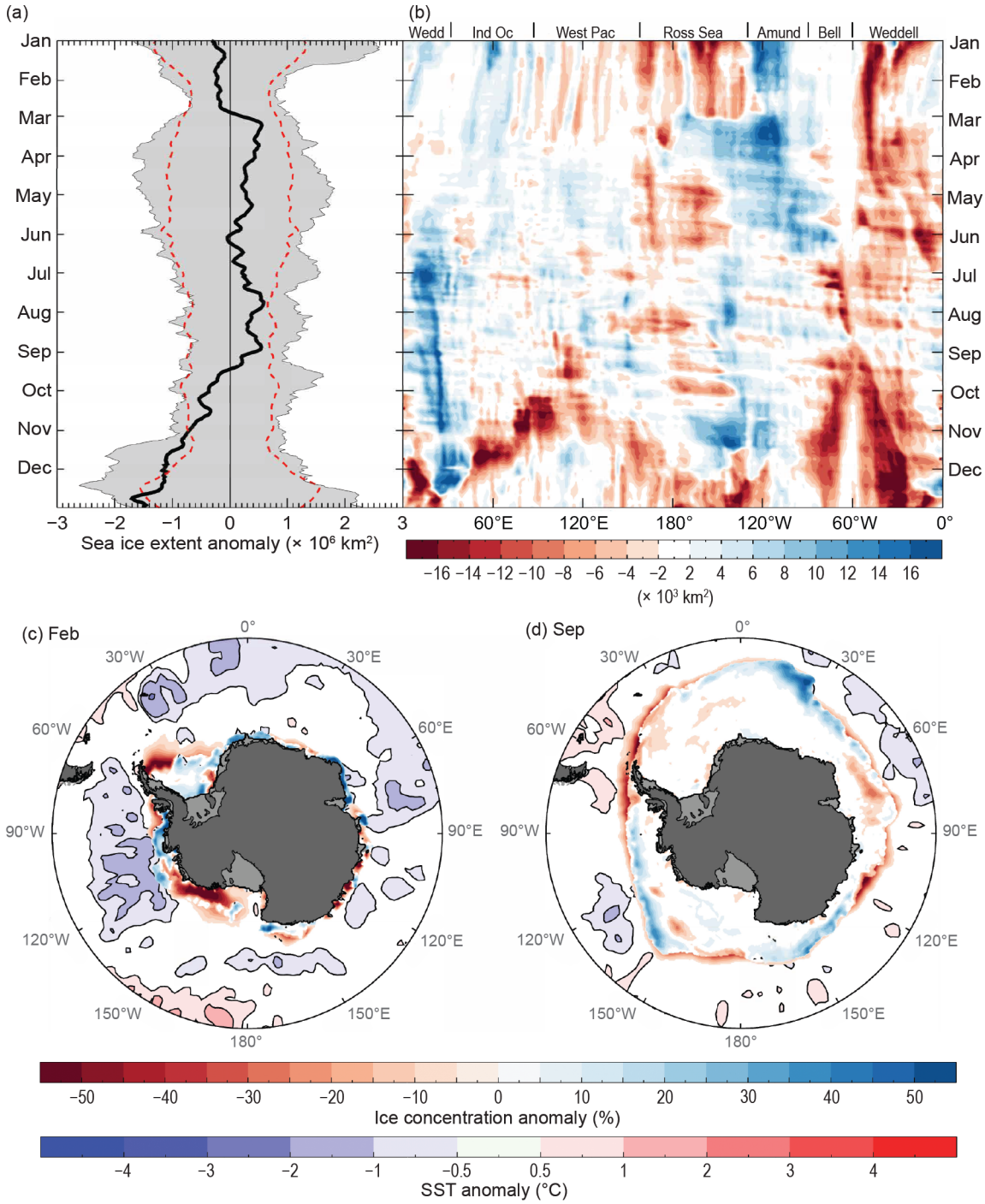

Fig. 6.11. (a) Time series of net daily SIE anomaly (× 10^6 km^2) for 2021 (solid black line) based on 1991–2020 climatology. The gray shading represents the historical (1979–2020) daily SIE anomaly. (b) Hovmöller (time–longitude) representation of daily SIE anomaly (× 10^3 km^2 per degree of longitude) for 2021. Maps of sea ice concentration anomaly (%) and SST anomaly (°C; Reynolds et al. 2002; Smith et al. 2008) for (c) Feb 2021 and (d) Sep 2021. Sea ice concentration is based on satellite passive-microwave ice concentration data (Cavalieri et al. 1996, updated annually, for climatology; Maslanik and Stroeve 1999), for the 2021 sea ice concentration. See Fig. 6.1 for relevant place names.

The low values of SIE and area during the early and then latter months of 2021 continue the recent trend towards decreased Antarctic sea ice coverage. Since 2015, 8 of the 12 calendar months have registered record low net Antarctic SIE (Parkinson and DiGirolamo 2021), but there are distinct regional and seasonal components to these events (Parkinson 2019; Stammerjohn and Maksym 2017). Overall, net Antarctic SIE has displayed substantial variability over the last decade, with record high values during 2012–14 (Reid and Massom 2015), followed by several years of low and record low values (Parkinson 2019; Reid et al. 2021). Through much of 2021, atmospheric anomalies were strong and distinct (section 6b), particularly the depth of the Amundsen Sea Low (ASL) from September onwards. However, given the pattern of generally sustained low sea ice coverage since 2016, it is quite probable that there are ocean influences predisposing the sea ice to early retreat (section 6g; Kusahara et al. 2018; Meehl et al. 2019). Below, we discuss four sequential phases of spatio-temporal progressions of Antarctic sea ice in 2021 based on the patterns and changes shown in Figs. 6.11a,b. These four sea ice phases (January–February, March–April, May–August, and September–December) reflect similar patterns in the atmospheric pressure and wind fields (section 6b) and sea surface temperatures (SSTs).

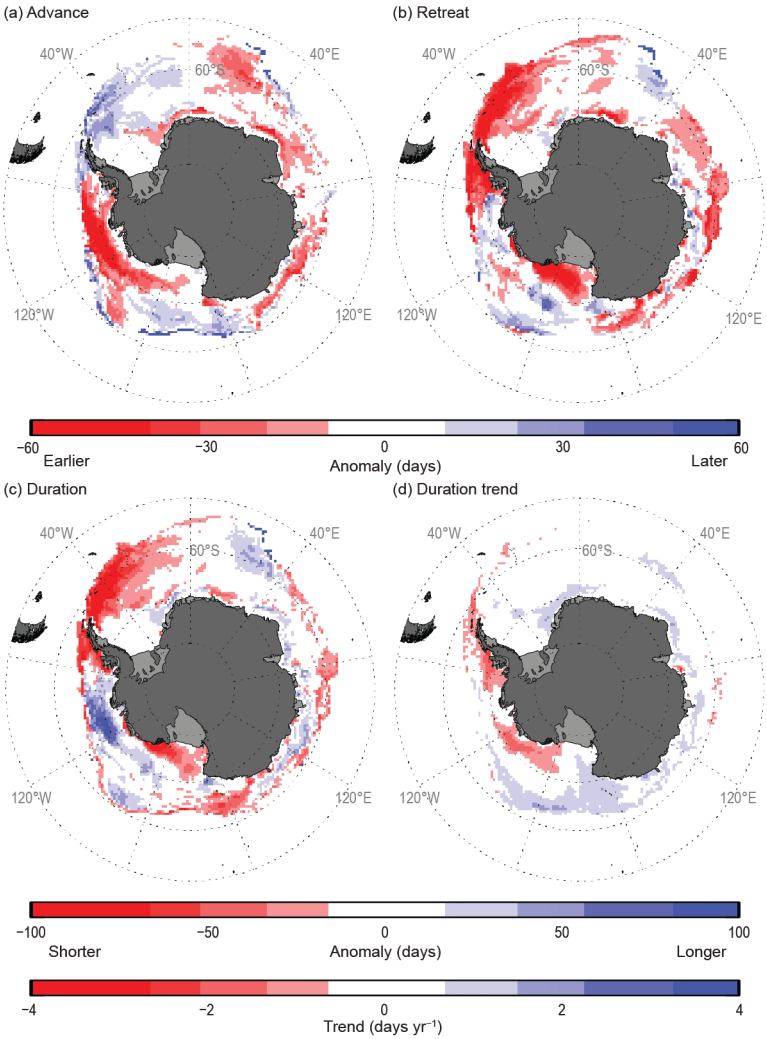

Fig. 6.12. Maps of seasonal sea ice anomalies (days) in 2021 during (a) autumn ice-edge advance, (b) spring ice-edge retreat, (c) winter ice season duration; together with (d) winter ice season duration trend (days yr^{-1}; Stammerjohn et al. 2008). The seasonal anomalies (a–c) are computed against the 1991/92 to 2020/21 climatology; the trend (d) is computed over 1979/80 to 2020/21. (Source: GSFC Bootstrap v3.1 daily data [Comiso 2017] through 31 May 2021, augmented with NASA Team NRTSI daily data [Meier et al. 2021] through 15 Feb 2022.)

As a continuation of the 2020/21 sea ice retreat process, regional patterns of sea ice coverage in January–February 2021 closely followed those of late 2020 (Reid et al. 2021). The regions of persistent high SIE and slower-than-normal seasonal retreat in the Indian Ocean off Dronning Maud Land (~0°–70°E) and in the Amundsen Sea (Fig. 6.11b, and reflected by an earlier advance in Fig. 6.12a) were consistent with below-average SSTs in those regions (Fig. 6.11c; section 6g). These cooler, icier regions were possibly due to the influence of two dominant atmospheric low-pressure anomalies (> 2.5 std. dev. below normal) at ~100°W and 40°E that contributed to the northward advection of cooler air and sea ice. Elsewhere, however, extensive faster-than-average sea ice retreat occurred across much of East Antarctica, the Ross Sea (~70°E–120°W), and the western Weddell Sea (~0°–60°W; Figs. 6.11b,c), leading to a net overall negative SIE anomaly (Fig. 6.11a).

During March, an abrupt change from a negative to a strongly positive anomaly in regional SIE took place in the eastern Ross Sea (Fig. 6.11b) in response to an eastward shift of a well-developed ASL (section 6b). This strong low-pressure anomaly and coincident below-normal SSTs (section

6g) led to rapid sea ice advance in the eastern Ross Sea and across the Amundsen Sea during March–April (Figs. 6.11b, 6.12a). At the same time, an extensive zone of anomalously persistent ice coverage at ~40°–70°E coincided with the southward incursion of a negative SST anomaly associated with a high-pressure anomaly centered on ~25°E. Elsewhere, a relatively slow autumn sea ice advance (Fig. 6.12a) led to negative SIE anomalies across the western Antarctic Peninsula through the Weddell Sea, and also in the western Ross Sea and southwest Pacific Ocean (Fig. 6.11b). In April, circum-Antarctic sea ice was strongly influenced by the development of a zonal wave-3 atmospheric pattern with low-pressure centers at ~40°E, 160°E, and 90°W (see Fig. 6.3e). At this time, the appearance of a predominantly positive SIE anomaly across much of East Antarctica (~0°–130°E) coincided with an increase in cyclonic activity there, and the positive anomaly in the far eastern Ross Sea and Amundsen Sea sector persisted as well. In contrast, SIE remained below average across the western Peninsula and western Weddell Sea and in the Ross Sea region.

During May–July, sea ice conditions were strongly affected by the redevelopment of a deep ASL (a typical La Niña response due to Rossby-wave activity; Yuan 2004) in concert with the persistent, but spatially variable, circumpolar atmospheric zonal wave-3 pattern (section 6b). As part of this pattern, the appearance in May of a deep low-pressure system off Enderby Land (centered on ~45°E) provided strong equatorward air flow that led to enhanced late-autumn sea ice advance (Fig. 6.12a) and a regional positive SIE anomaly that persisted in the eastern limb of the Weddell Gyre through mid-December (Fig. 6.11b). Sea ice advance was also earlier than average across much of East Antarctica west of ~150°E, with persistence of a zonally-extensive positive SIE anomaly from May through July (Fig. 6.11b), likely a result of stronger-than-normal westerly winds due to the combination of low-pressure systems to the south of the sea ice edge and a high-pressure ridge to the north (section 6b). SIE also remained larger than normal in the Amundsen Sea region, but smaller-than-average in the Bellingshausen, western Weddell, and Ross Seas (Fig. 6.11b). This regional pattern of circum-Antarctic anomalies in SIE remained through August, after which there was a development of a more zonally consistent pattern of circumpolar lows (see Fig. 6.3g).

The period of September–December was characterized by an abrupt downturn in overall net SIE around Antarctica (Fig. 6.11a) as a result of zonally-extensive negative SIE anomalies in the Indian and West Pacific Oceans, Bellingshausen through western Weddell Seas, and latterly the Ross Sea (Figs. 6.11b,d). This pattern of anomalously early sea ice retreat (in all sectors apart from the outer eastern Weddell Sea, outer eastern Ross Sea, and portions of the Bellingshausen-Amundsen sector between 80°W and 120°W; Fig. 6.12b) was strongly influenced by a re-emergence and deepening of the ASL in September, which persisted to the end of the year (section 6b). Prevailing warm northerly winds in the eastern part of the ASL particularly impacted the western Peninsula region and western Weddell Sea (~0°–90°W), where SIE was 1–3 std. dev. below the mean from September to the end of the year. Due to the prevalence of cold southerly winds in the western flank of the ASL in the Amundsen and eastern Ross Seas (~90°–150°W), SIE remained predominantly larger than normal until December, at which time it started to retreat rapidly. The exception was the northern Amundsen Sea, where SIE remained above average through to the end of the year (Fig. 6.11b). The continuation of a strong negative SIE anomaly and rapid sea ice retreat in the West Pacific sector in October (Figs. 6.11b, 6.12b) coincided with the development of a major high-pressure anomaly centered offshore at ~170°E. For much of East Antarctica and from September onwards, sea ice retreated rapidly (Fig. 6.12b) and at times regional (~50°–100°E) SIE was 3–4 std. dev. below average. By the end of the year, only the eastern Amundsen Sea and small embayments across East Antarctica showed larger-than-average SIE (not shown).

Large regional anomalies in seasonal advance and retreat combine to produce a distinct pattern of ice season duration anomalies (Fig. 6.12c), with the western Antarctic Peninsula and much of the outer Weddell and inner Ross seas experiencing a much shorter ice season duration by more than 50 days. The shorter ice season along the western Antarctic Peninsula and eastern

Ross Sea are consistent with their long-term trends, in contrast to the ice season anomalies in the Bellingshausen-Amundsen region between 80°W and 120°W and the western Ross Sea, both of which were opposite to their long-term trends (Figs. 6.12 c,d).

g. Southern Ocean—R. L. Beadling, N. M. Freeman, G. A. MacGilchrist, M. Mazloff, J.-R. Shi, A. F. Thompson, and E. Wilson

The Southern Ocean (SO) moderates the climate system as a vast, but variable, sink for anthropogenic heat (Frölicher et al. 2015; Shi et al. 2018) and carbon dioxide (CO_2, Frölicher et al. 2015). Additionally, nutrients upwelled in the subpolar SO and advected northward fertilize three quarters of global ocean biological productivity (Sarmiento et al. 2004). Motivated by their imprint on the climate system through their role in the SO heat and carbon budget, we present 2021 anomalies of SO sea surface temperature (SST), mixed layer (ML) properties, ocean heat content (OHC), and surface chlorophyll concentration. The state of the SO in 2021 was characterized by zonally-asymmetric SST anomalies, near-record positive anomalies in ML salinity (MLS) and ML depth (MLD) in portions of the SO, a continued increase in ocean heat content (OHC), accelerated upper ocean zonal flow, and near-record summer chlorophyll concentrations.

1) SEA SURFACE TEMPERATURE AND MIXED LAYER PROPERTIES

Southern Ocean SST and ML properties in 2021 are analyzed with respect to the 2004–20 period. Monthly SST data are from the NOAA Optimum Interpolation (OISST) V2 product (Reynolds et al. 2002), while ML properties are from the Argo-based Roemmich-Gilson dataset (Roemmich and Gilson 2009; RG09). We focus on 40°–65°S since this region encapsulates variations around the Antarctic Circumpolar Current (ACC). Following the de Boyer Montegut et al. (2004) threshold method, MLD is defined as the depth at which potential density changes by the threshold value of 0.03 kg m^{-3} relative to the 10-m surface reference value.

In 2021, SO SST anomalies exhibited a distinct zonal asymmetry, with anomalies largely compensating in the zonal mean (Figs. 6.13a,b). Anomalous cooling spanned the central Atlantic to central Indian Oceans and across the eastern Pacific, while anomalous warming was prominent across the western portions of the Pacific and Atlantic. These anomaly patterns are consistent with the Southern Annular Mode (SAM) being in a strongly positive state for much of 2021 (section 6b; Sallée et al. 2010). Zonal-mean MLS approached record highs (~0.02 g kg^{-1}) toward the end of 2021, with large anomalies in the South Atlantic (Figs. 6.13c,d). This may be viewed as a resumption of the higher-than-normal MLS that persisted from 2015 to 2020. Possible factors contributing to the high MLS include the reduction in Antarctic SIE (section 6f), a poleward shift of precipitation away from midlatitudes associated with a more southerly storm track during the positive SAM phase, and a stronger South Atlantic subtropical gyre. A stronger gyre implies increased transport of saline sub-tropical waters to the region. Sea surface height (SSH) maps from Archiving, Validation, and Interpretation of Satellites Oceanographic Data (AVISO; www.aviso.altimetry.fr/duacs/) support a continued (Qu et al. 2019) spin-up of this gyre, with 2021 mean SSH magnitudes ~2 cm greater in the center of the gyre relative to the 1993–2020 climatology (Southern Hemisphere spatially-averaged trend was first removed; not shown here). Distinguishing between these plausible mechanisms would require a thorough salinity budget analysis. Deep winter MLDs (anomalies > 100 m) were found across the southeastern Pacific in 2021 (Fig. 6.13e,f), comparable to the record MLD anomalies that occurred in 2010. Similar to 2010, 2021 was dominated by a positive SAM, which favors deeper winter mixed layers in the southeastern Pacific (Fogt et al. 2011; Sallée et al. 2010) increasing local ocean ventilation and creating conditions conducive to enhanced mode water formation in the region (MacGilchrist et al. 2021; Morrison et al. 2022).

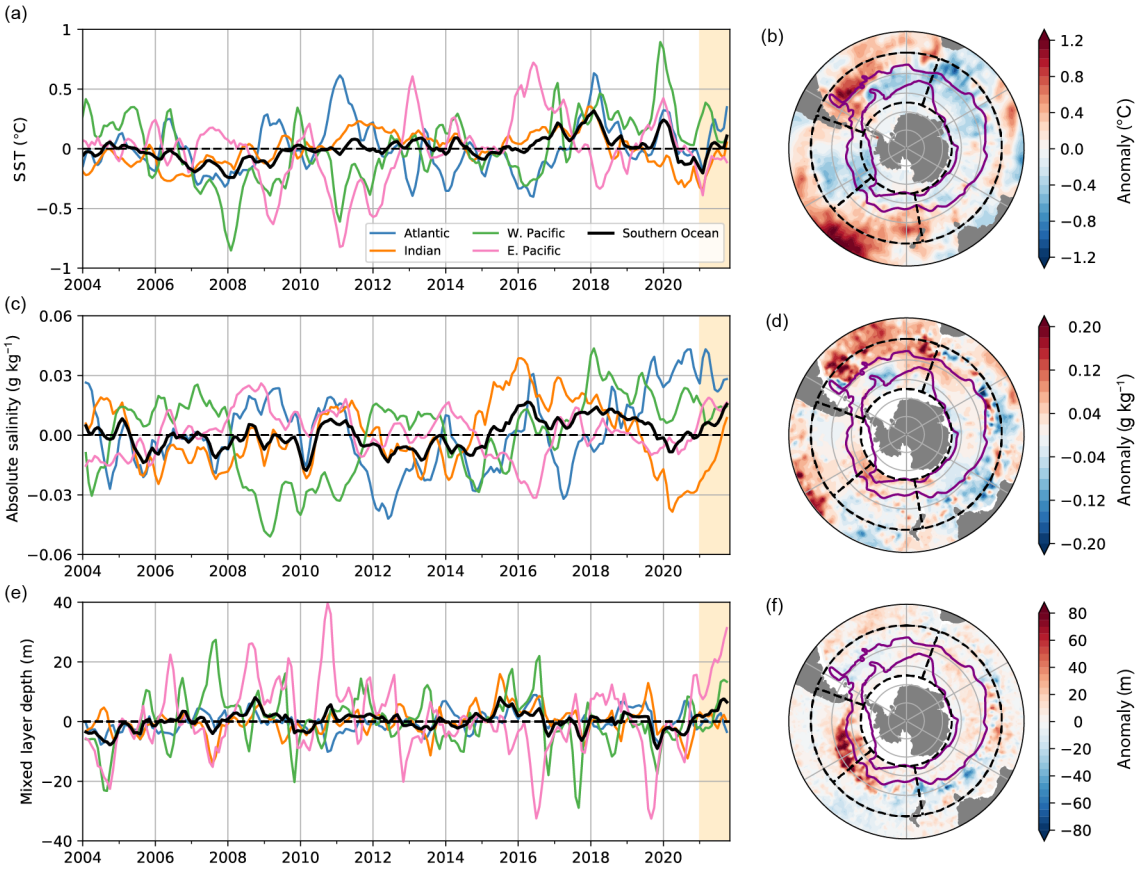

Fig. 6.13. Monthly averaged (a,b) sea surface temperature (SST; °C), (c,d) mixed layer absolute salinity (g kg^{-1}), and (e,f) mixed layer depth anomalies (m) for the SO. Left column: anomaly time series. Right column: corresponding annual mean anomaly maps for 2021, where purple contours outline the subantarctic and southern ACC Fronts as defined by Orsi et al. (1995). Regions highlighted in the anomaly time series correspond to the regional boundaries (SO, Atlantic, Indian, West Pacific, and East Pacific) defined by the dashed lines in the anomaly maps spanning 40°–65°S. Anomalies are computed relative to the 2004–20 monthly climatology and smoothed using a 3-month moving average. 2021 is highlighted with yellow shading on each time series (a,c,e).

2) OCEAN HEAT CONTENT AND ZONAL FLOW

We use monthly gridded temperature data from RG09 to evaluate 0 to 2000-m SO (south of 30°S) OHC and subsurface potential temperature anomalies relative to the 2005–20 climatological seasonal cycle. In 2021, the SO annual mean upper 2000-m OHC anomaly was +28.9 ZJ (10^{21} J) (Fig. 6.14a), increasing by ~2.5 ZJ compared to 2020. South of 40°S, the OHC anomaly was +19.8 ZJ, increasing by 0.1 ZJ compared to 2020. These increases in OHC relative to 2020 are smaller than the interannual variability (5.0 ZJ south of 30°S; 2.3 ZJ south of 40°S) estimated from the std. dev. of the detrended annual OHC during 2005–21. The long-term positive trend in OHC reflects continued multi-decadal subsurface warming in the SO and is consistent with the 2021 global OHC increase (Cheng et al. 2022). Most of the enhanced OHC occurred north of the ACC, with pronounced positive anomalies in the South Atlantic and southwest Pacific around western boundary currents (Fig. 6.14b). The coherence between the strong positive Atlantic OHC and MLS anomalies is consistent with a spin-up of the South Atlantic gyre. The 2021 OHC anomalies were negligible within and south of the ACC where the upwelling of cool deep waters to the upper ocean mitigates the anthropogenic warming signal. This spatial asymmetry in SO OHC anomalies resulted in a north–south gradient in subsurface potential temperature anomalies (Fig. 6.14c), with maximum warming peaking around 46°–50°S below 100 m. Consistent with the enhanced meridional temperature gradient, the baroclinic component of SO eastward flow

in 2021 accelerated within 48°–58°S (Shi et al. 2020, 2021). Weak negative anomalies (~0.1°C) in subsurface temperature were found at depths of about 100 m south of 55°S, which may be related to an anomalous northward Ekman transport of sea ice (Haumann et al. 2020) associated with the positive SAM phase in 2021.

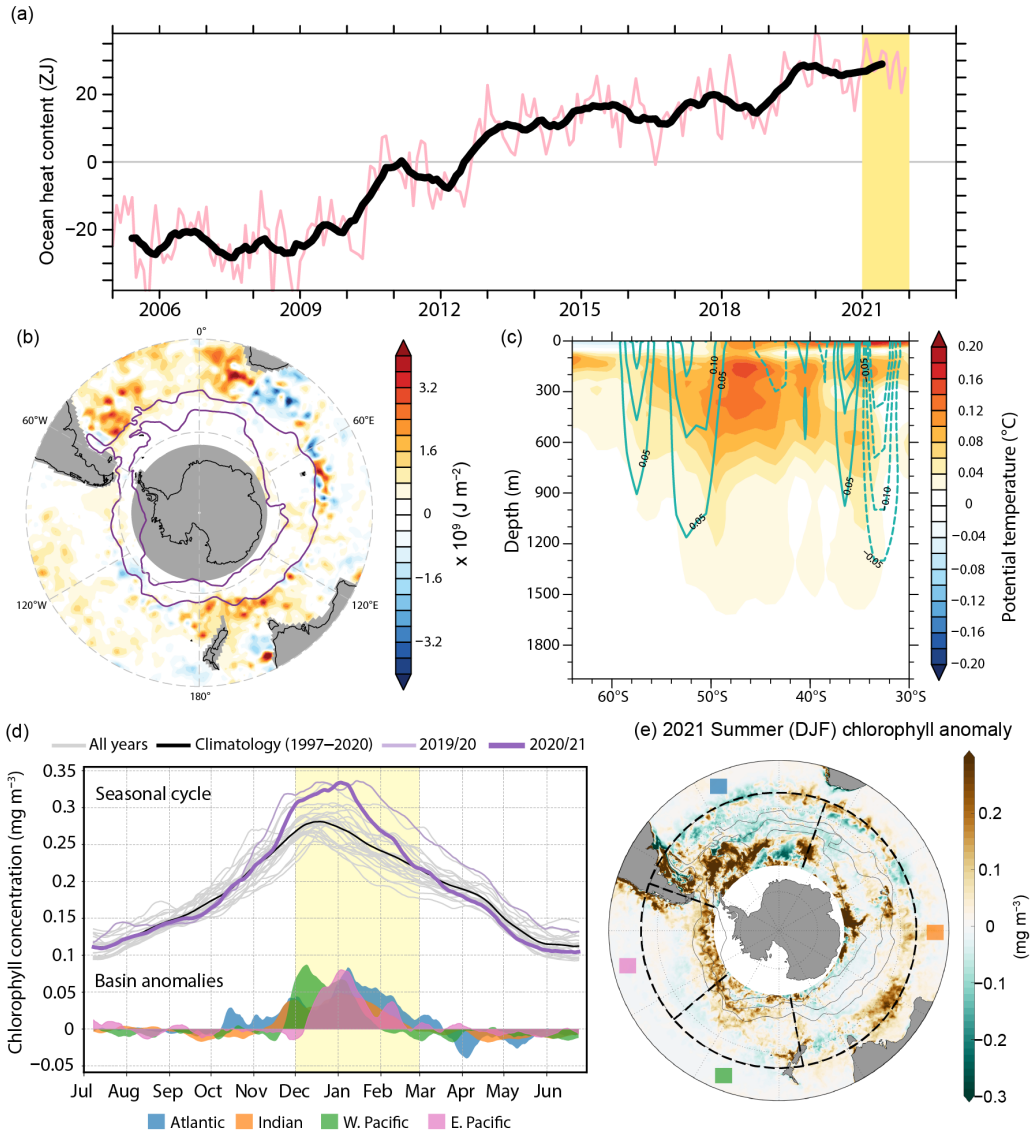

Fig. 6.14. (a,b) 2021 anomalies of upper 2000-m OHC relative to 2005–20 Argo climatology. (a) Time series of monthly mean OHC anomaly (ZJ or 10^{21} J) relative to 2005–20 Argo climatology south of 30°S (pink curve) with 12-month running mean plotted on top (black curve) and 2021 highlighted in yellow shading. (b) Map of 2021 OHC anomalies (10^9 J m^{-2}) relative to climatology (2005–20) with the mean position of the subantarctic and southern ACC Fronts from Orsi et al. (1995) contoured in purple. (c) SO Zonal mean 2021 potential temperature anomalies (°C) with the 2021 zonal geostrophic velocity anomalies contoured in green. Solid contours represent eastward anomalies and dashed are westward anomalies. (d, top section) Seasonal cycle of the area-weighted (40°–65°S), daily (arithmetic) mean chlorophyll concentration (mg m^{-3}): all historical years (1997–2020), the climatological mean (1997–2020), and the most recent 2019/20 and 2020/21 growing seasons. A 14-day rolling average filter was applied to the daily GlobColour product, a spatially and temporally interpolated ("cloud-free") multi-satellite merged product (https://doi.org/10.48670/moi-00100). Missing days were linearly interpolated; for weighted-averaging purposes, grid locations that are not resolved via satellite, particularly in data-sparse winter, are set to zero. (d, bottom section) Chlorophyll anomalies (mg m^{-3}) in 2020/21 contributed by each ocean basin, where the anomaly is computed relative to the climatology of that basin, delineated as in Fig. 6.13. The x-axis in (d) is centered on the austral summer months of Dec, Jan, and Feb (DJF), highlighted with vertical yellow shading. (e) Map of 2020/21 DJF chlorophyll anomalies (30°–65°S), computed relative to the 1997–2020 DJF climatology, using the monthly version of the GlobColour product. Overlain are zonal and meridional (dashed) outlines of the subdivided ocean basins (d, 40°–65°S) and, from north to south, the subantarctic, polar, and southern ACC fronts (solid gray contours; Orsi et al. 1995).

3) SURFACE CHLOROPHYLL

Chlorophyll concentration in the open (ice free) ocean is examined using the GlobColour merged ocean color product (L4 daily and monthly at 4 km; September 1997–June 2021; Fanton d'Andon et al. 2009; Maritorena et al. 2010), with 2021 anomalies computed relative to the 1997–2020 climatology. SO phytoplankton abundance (indicated by surface chlorophyll concentration) exhibited anomalous seasonal variability during the 2020/21 growing season (July 2020–June 2021; Figs. 6.14d,e). The pronounced 2020/21 austral summer (DJF) peak joins the 2019/20 season as the two highest chlorophyll summers observed in the GlobColour record (Fig. 6.14d). The 2020/21 growing season began at near-normal winter–spring chlorophyll levels, followed by anomalously rapid summer growth beginning in mid-November, reaching a maximum in early January (> 0.3 mg m^{-3}), the largest in the GlobColour record (Fig. 6.14d). Following the summer peak, chlorophyll concentration quickly declined to anomalously low levels in most regions by mid-March, remaining consistently below climatological values throughout the autumn–winter transition (Fig. 6.14d).

Phytoplankton in the Atlantic, Indian, and west Pacific sectors accounted for most of the rapid growth from mid-November (Fig. 6.14d), after which, anomalously high chlorophyll was maintained through DJF by strong, positive anomalies across all sectors (Figs. 6.14d,e). Across the SO, the strongest positive anomalies were found south of the Subantarctic Front, most notably in the Pacific and Atlantic basins (Fig. 6.14e). The deep Amundsen Sea Low and strong positive SAM (section 6b) created conditions conducive to the upwelling of nutrients in support of an invigoration of the spring bloom. In the Atlantic, most of the basin-wide chlorophyll increase was concentrated east of Drake Passage near the Scotia Arc (Fig.6.14e).

h. 2021 Antarctic ozone hole—N. A. Kramarova, P. A. Newman, E. R. Nash, S. E. Strahan, B. Johnson, M. Pitts, M. L. Santee, I. Petropavlovskikh, L. Coy, and J. De Laat

The 2021 Antarctic ozone hole was the 13th largest in 42 years of satellite observations since 1979, with an area of 23.34×10^6 km^2 (the average area for 7 September–13 October) and a minimum daily total ozone column of 92 DU. The 2021 polar stratospheric vortex was stable with consistently cold temperatures that created favorable conditions for ozone depletion. The meteorological conditions and seasonal development of the ozone hole in 2021 were similar to those in 2020. Weaker-than-usual amplitudes of planetary scale Rossby waves in the September–October period helped maintain a strong vortex and led to below-average Antarctic ozone columns in late austral spring and early summer.

Antarctic lower stratospheric temperatures were consistently near- or below average during austral winter and spring 2021 (Fig. 6.15a). Cold air facilitated formation of polar stratospheric clouds (PSCs; Fig. 6.15b), whose spatial volume was near-average in July–August and above average in September. PSC particles provide surfaces for heterogeneous chemical reactions that release active chlorine (Cl_2) for ozone depletion as sunlight returns to polar latitudes in August–September. Concentrations of ClO (Fig. 6.15c) were near- or below average until mid-September and above average in early October, similar to those in 2020. *Aura* Microwave Limb Sounder (MLS) observations showed that the 2021 vortex-averaged ozone concentration (Fig. 6.15d) on the 440-K isentropic surface (~60 hPa) was substantially above the average. However, the change in ozone concentration between the first week of July and the first week of October indicated that seasonal ozone losses were about 2.22 ppmv, which is comparable to the losses in two other cold years: 2.18 ppmv in 2020 and 2.24 ppmv in 2006. The Antarctic ozone hole area, defined by the region with total ozone columns below 220 DU, reached its peak at 24.8×10^6 km^2 on 7 October (Fig. 6.15e). The weaker-than-average amplitudes of planetary scale Rossby waves through austral spring (which propagate from the upper troposphere into the stratosphere, depositing momentum and warming the Antarctic stratosphere) produced colder temperatures inside the vortex and inhibited mixing across the vortex edge, allowing the ozone hole area to remain well above the average until it disappeared on 23 December. This was one of the longest-lasting ozone holes on

record, second only to 2020 (Kramarova et al. 2021). In 2006 (orange line in Fig. 6.15e), the area of the ozone hole grew faster in August–September partly because the level of ozone depleting substances was ~3.7 ppbv, which is 0.4 ppbv higher than today (NASA 2022). Below-average temperatures in 2006 resulted in the largest ozone hole on record. The slower growth rate of the 2021 ozone hole is consistent with other indications of recovery, such as the delayed onset of the hole's appearance and its decreasing size in September, all attributable to decreasing levels of ozone depleting substances (Stone et al. 2021).

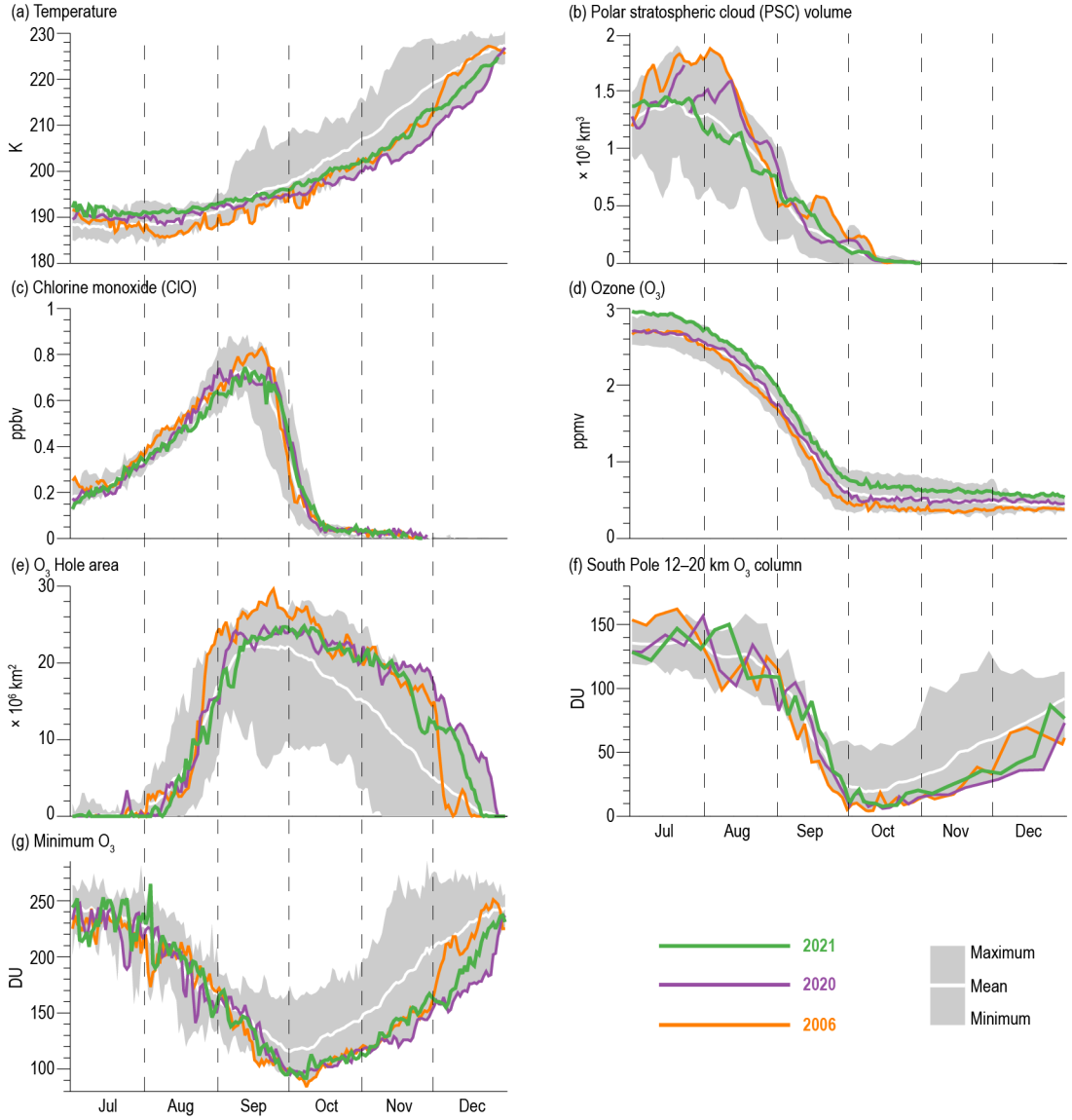

Fig. 6.15. Antarctic values of (a) vortex-averaged MERRA-2 temperature (K), (b) CALIPSO PSC volume (× 10^6 km^3) updated from Pitts et al. (2018), (c,d) vortex-averaged ClO (ppbv) and O_3 (ppmv) measured by Aura MLS (updated from Manney et al. 2011), (e) OMI/OMPS Antarctic ozone hole area (× 10^6 km^2, area with ozone total column less than 220 DU), (f) lower stratospheric ozone columns (DU, 12–20 km) based on sonde measurements at South Pole, and (g) minimum total ozone columns (DU) over 60°–90°S from OMI/OMPS. MERRA-2 temperature and MLS averages are made inside the polar vortex on the 440-K potential temperature surface (~19 km or 60 hPa). Gray shading shows the range of daily Antarctic values for 2005 (for all but (b), which starts in 2006) through 2020. The white curve indicates the 2005–20 long-term mean.

Sonde observations at South Pole station indicated that the lower stratospheric column between 12 and 20 km was near-average in July–September (Fig. 6.15f) but was below average from October through December. The lowest 12–20-km column measured was 7.6 DU on 15 October, about two weeks later than in most years. The minimum total column ozone over the Antarctic (60°–90°S) were detected on 7 and 8 October at 92 DU, and minimum total ozone columns were also consistently below the average from mid-September to December. This seasonal behavior is similar to that in 2006 and 2020 (orange and purple lines in Fig. 6.15, respectively)—the two prior years with similarly weak wave activity and cold temperatures that resulted in persistently large holes and low ozone columns in October–December. The ClO concentration and PSC volumes dropped to near zero by mid-October (Figs. 6.15b,c), marking the termination of seasonal ozone depletion (Fig. 6.15d), but the stable vortex in 2021 kept ozone columns below average for the rest of the year by preventing meridional mixing of ozone-rich air from the midlatitude stratosphere into polar latitudes.

September is the key time period for Antarctic ozone depletion (e.g., Strahan et al. 2019). As the sunlight returns to polar latitudes, catalytic ozone destruction is initiated by reactions with active chlorine and bromine species produced on PSC surfaces during polar night. Colder September temperatures increase PSC surface area, leading to greater ozone depletion and a larger hole area. Figure 6.16a shows the interannual variability in the September vortex temperature with the

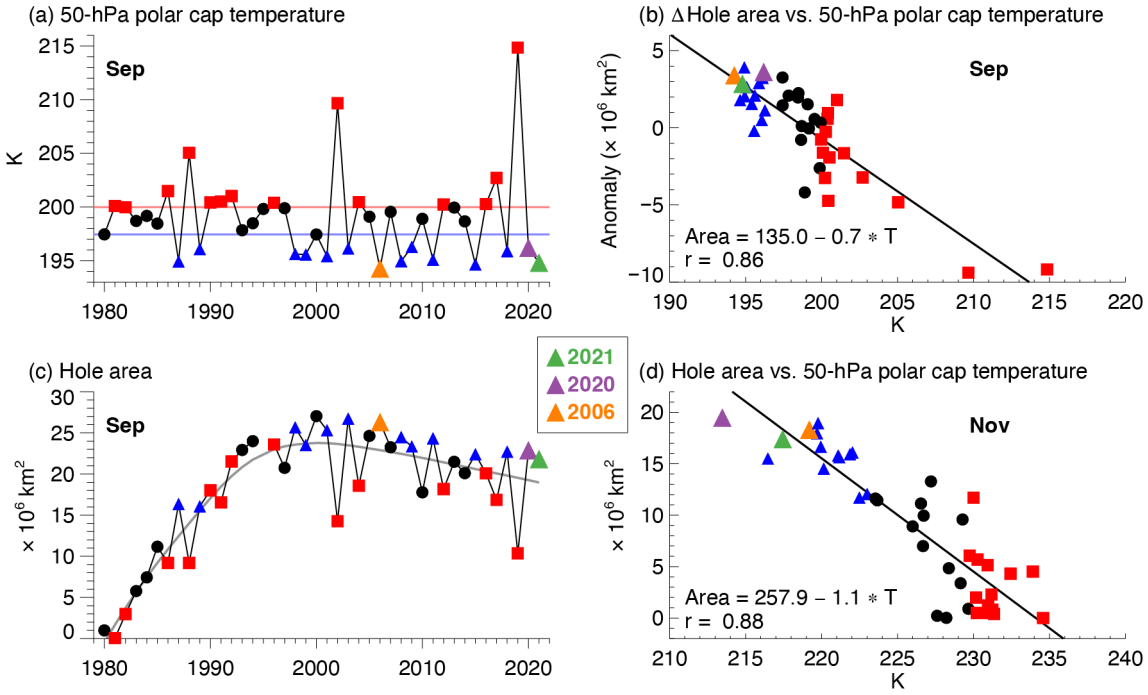

Fig. 6.16. (a) MERRA-2 50-hPa Sep temperature (K) averaged over 60°–90°S, (b) inter-annual anomalies of the ozone hole area (× 10^6 km^2) in Sep (see text) vs. 50-hPa temperature (K), (c) Sep average Antarctic ozone hole area (× 10^6 km^2), and (d) Nov ozone hole areas (× 10^6 km^2) vs. 50-hPa Nov temperature (K). Years with temperatures in the lowest (highest) third are shown as blue triangles (red squares), and three cold years 2006, 2020, and 2021 are highlighted in orange, purple, and green, respectively. The horizontal blue and red lines in (a) indicate 33% and 66% percentiles. The gray curve in (c) shows a quadratic fit of EESC with a 5.2 year mean age (Newman et al. 2007) to the Sep hole areas. Ozone data for 1979–92 are from Total Ozone Mapping Spectrometer (TOMS) Nimbus-7, 1993–94 are from TOMS Meteor-3, 1996–2004 are from EPTOMS, 2005–15 are from *Aura* Ozone Monitoring Instrument (OMI), and 2015–21 are from Suomi National Polar-orbiting Partnership (SNPP) Ozone Mapping and Profiler Suite (OMPS). There were no satellite total ozone observations for 1995. The black lines in (b) and (d) show the linear fit, with a correlation of 0.86 and 0.88 (statistically significant at > 99.9% confidence level) for Sep and Nov, respectively.

coldest one-third of years shown in blue. The September ozone hole area also depends on levels of active chlorine (Fig. 6.16c). The effective equivalent stratospheric chlorine (EESC) represents an estimated concentration of human-produced and natural chlorine and bromine compounds in the stratosphere (Newman et al. 2007). EESC concentration reached its maximum level in the early 2000s and declined thereafter because of the implementation of the Montreal Protocol and its amendments. EESC levels were 13% lower in 2021 compared to the maximum. The impact of the slow rate of EESC decline on the ozone hole area is only observable on decadal or longer timescales, while the interannual variations are modulated by lower stratospheric temperatures: the ozone hole is larger in colder years and smaller in warmer years (Fig. 6.16c). To isolate the temperature effect, we fit a quadratic function of EESC with a 5.2 year mean age (shown as gray line in Fig. 6.16c) to the observed ozone hole areas, then determined the relationship between temperature and the deviation of the observed area from the fitted area (Fig. 6.16b). The September area anomalies are highly correlated with September temperatures ($r = 0.86$, Fig. 6.16b). Thus, the above-average area in September 2021 was largely the result of below-average temperatures.

Ozone depletion ceased by mid-October (Fig. 6.15d) because the ClO concentration and PSC volume dropped to near zero (Figs. 6.15b,c). Therefore, the ozone hole area in November fully depended on cold meteorological conditions that allowed the ozone-depleted air mass to persist over Antarctica. Figure 6.16d demonstrates a strong linear dependence between the area of the November ozone hole and lower stratospheric temperatures in November ($r = 0.88$).

While the 2021 Antarctic ozone hole was larger than average, it was smaller than ozone holes in the late 1990s and 2000s when the levels of ozone depleting substances were near their maximum. The weak amplitudes of planetary scale waves throughout spring 2021 slowed the winter-to-summer transition, resulting in one of the longest-lived ozone holes in the observational record. These results demonstrate that the changes in the Antarctic ozone hole area are consistent with our understanding of ozone depletion, and that ozone recovery due to the implementation of the Montreal Protocol has emerged despite large interannual fluctuations in stratospheric dynamics.

Acknowledgements

- N. M. Freeman was supported by the NASA Ocean Vector Winds Science Team (NASA award 80NSSC19K0059).
- R. L. Fogt acknowledges support from the National Science Foundation grant OPP-1744998.
- M. A. Lazzara, L. M. Keller, and T. Norton were supported in part by the National Science Foundation Grant OPP-1924730.
- K. R. Clem acknowledges support from the Royal Society of New Zealand Marsden Fund grant MFP-VUW2010.
- J. D. Wille acknowledges support from the Agence Nationale de la Recherche projects ANR-20-CE01-0013 (ARCA).
- R. T. Datta acknowledges support from the National Science Foundation, Award No. 1952199
- E. Wilson acknowledges support from Caltech's Terrestrial Hazard Observations and Reporting (THOR) Center.
- A. F. Thompson acknowledges support from NASA Jet Propulsion Laboratory's Internal Research and Development program, Earth 2050.
- G. A. MacGilchrist and M. Mazloff acknowledge support from NSF's Southern Ocean Carbon and Climate Observations and Modeling (SOCCOM) Project under NSF Award PLR-1425989, with additional support from NOAA and NASA. Logistical support for SOCCOM in the Antarctic was provided by the U.S. NSF through the U.S. Antarctic Program.
- Work at the Jet Propulsion Laboratory, California Institute of Technology, was done under contract with the National Aeronautics and Space Administration (NASA). Support was also provided by the NASA Modeling and Analysis Program. We are indebted to the many NOAA Corps Officers and GML technical personnel who spend the winters at South Pole Station to obtain the ongoing balloon and ground-based data sets. We also acknowledge the logistics support in Antarctica provided by the National Science Foundation Office of Polar Programs.
- Section 6h: © 2022. All rights reserved.
- P. Reid and J. Lieser were supported through the Australian Bureau of Meteorology, and R. Massom by the Australian Antarctic Division. The work of P. Reid and R. Massom also contributes to the Australian Government's Australian Antarctic Partnership Program (AAPP). For R. Massom, this work was also supported by the Australian Research Council Special Research Initiative the Australian Centre for Excellence in Antarctic Science (Project Number SR200100008).
- S. Stammerjohn was supported under NSF PLR 1440435; she also thanks the Institute of Arctic and Alpine Research and the National Snow and Ice Data Center, both at the University of Colorado Boulder, for institutional and data support.
- S. Barreira was supported by the Argentine Naval Hydrographic Service.
- T. Scambos was supported under NASA grants NNX14AM54G and 80NSSC21K0750, the Arctic Sea Ice News and Analysis project and NSF ANT 1738992, and the NSF-NERC International Thwaites Glacier Collaboration TARSAN project.

Appendix 1: Chapter 6 – Acronyms

ACC	Antarctic Circumpolar Current
AIS	Antarctic ice sheet
AP	Antarctic Peninsula
AR	atmospheric river
ASL	Amundsen Sea Low
AWS	automated weather stations
CL_2	chlorine
ClO	chlorine monoxide
CO_2	carbon dioxide
EESC	effective equivalent stratospheric chlorine
ENSO	El Niño–Southern Oscillation
ML	mixed layer
MLD	mixed layer depth
MLS	Microwave Limb Sounder
MSLP	mean sea level pressure
NSIDC	National Snow and Ice Data Center
OMI	ozone monitoring instrument
PSC	polar stratospheric cloud
SAM	Southern Annular Mode
SIE	sea ice extent
SMB	surface mass balance
SNPP OMPS	Suomi National Polar-orbiting Partnership/Ozone Mapping and Profiler
SO	Southern Ocean
SOCCOM	Southern Ocean Carbon and Climate Observations and Modeling
std. dev.	standard deviation
w.e.	water equivalent
WAIS	West Antarctic ice sheet

References

Adusumilli, S., H. A. Fricker, B. Medley, L. Padman, and M. R. Siegfried, 2020: Interannual variations in meltwater input to the Southern Ocean from Antarctic ice shelves. *Nat. Geosci.*, **13**, 616–620, https://doi.org/10.1038/s41561-020-0616-z.

——, A. M. Fish, H. A. Fricker, and B. Medley, 2021: Atmospheric river precipitation contributed to rapid increases in surface height of the west Antarctic ice sheet in 2019. *Geophys. Res. Lett.*, 48, e2020GL091076, https://doi.org/10.1029/2020GL091076.

Agosta, C., and Coauthors, 2019: Estimation of the Antarctic surface mass balance using the regional climate model MAR (1979–2015) and identification of dominant processes. *Cryosphere*, **13**, 281–296, https://doi.org/10.5194/tc-13-281-2019.

Alley, K. E., and Coauthors, 2021: Two decades of dynamic change and progressive destabilization on the Thwaites Eastern Ice Shelf. *Cryosphere*, **15**, 5187–5203, https://doi.org/10.5194/tc-15-5187-2021.

Aublanc, J., P. Thibaut, A. Guillot, F. Boy, and N. Picot, 2021: Ice sheet topography from a new CryoSat-2 SARIn processing chain, and assessment by comparison to ICESat-2 over Antarctica. *Remote Sens.*, **13**, 4508, https://doi.org/10.3390/rs13224508.

Banwell, A. F., D. R. MacAyeal, and O. V. Sergienko, 2013: Breakup of the Larsen B ice shelf triggered by chain reaction drainage of supraglacial lakes. *Geophys. Res. Lett.*, **40**, 5872–5876, https://doi.org/10.1002/2013GL057694.

——, R. T. Datta, R. L. Dell, M. Moussavi, L. Brucker, G. Picard, C. A. Shuman, and L. A. Stevens, 2021: The 32-year record-high surface melt in 2019/2020 on the northern George VI Ice Shelf, Antarctic Peninsula. *Cryosphere*, **15**, 909–925, https://doi.org/10.5194/tc-15-909-2021.

Barrand, N. E., D. G. Vaughan, N. Steiner, M. Tedesco, P. Kuipers Munneke, M. R. Van den Broeke, and J. S. Hosking, 2013: Trends in Antarctic Peninsula surface melting conditions from observations and regional climate modeling. *J. Geophys. Res. Earth Surf.*, **118**, 315–330, https://doi.org/10.1029/2012JF002559.

Becker, M. K., S. L. Howard, H. A. Fricker, L. Padman, C. Mosbeux, and M. R. Siegfried, 2021: Buoyancy-driven flexure at the front of Ross Ice Shelf, Antarctica, observed with ICESat-2 laser altimetry. *Geophys. Res. Lett.*, **48**, e2020GL091207, https://doi.org/10.1029/2020GL091207.

Cavalieri, D. J., C. L. Parkinson, P. Gloersen, and H. J. Zwally, 1996: Sea ice concentrations from Nimbus-7 SMMR and DMSP SSM/I-SSMIS passive microwave data, version 1. NASA National Snow and Ice Data Center Distributed Active Archive Center, accessed 4 January 2022, https://doi.org/10.5067/8GQ8LZQVL0VL.

Cheng, L., and Coauthors, 2022: Another record: Ocean warming continues through 2021 despite La Niña conditions. *Adv. Atmos. Sci.*, **39**, 373–385, https://doi.org/10.1007/s00376-022-1461-3.

Clem, K. R., B. R. Lintner, A. J. Broccoli, and J. R. Miller, 2019: Role of the South Pacific convergence zone in West Antarctic decadal climate variability. *Geophys. Res. Lett.*, **46**, 6900–6909, https://doi.org/10.1029/2019GL082108.

——, R. L. Fogt, J. Turner, B. R. Lintner, G. J. Marshall, J. R. Miller, and J. A. Renwick, 2020: Record warming at the South Pole during the past three decades. *Nat. Climate Change*, **10**, 762–770, https://doi.org/10.1038/s41558-020-0815-z.

Comiso, J. C., 2017: Bootstrap sea ice concentrations from Nimbus-7 SMMR and DMSP SSM/I-SSMIS, version 3. NASA National Snow and Ice Data Center Distributed Active Archive Center, accessed 4 January 2022, https://doi.org/10.5067/7Q8HCCWS4I0R

Datta, R. T., and B. Wouters, 2021: Supraglacial lake bathymetry automatically derived from ICESat-2 constraining lake depth estimates from multi-source satellite imagery. *Cryosphere*, **15**, 5115–5132, https://doi.org/10.5194/tc-15-5115-2021.

de Boyer Montegut, C., G. Madec, A. S. Fischer, A. Lazar, and D. Iudicone, 2004: Mixed layer depth over the global ocean: An examination of profile data and a profile-based climatology. *J. Geophys. Res.*, **109**, C12003, https://doi.org/10.1029/2004JC002378.</jrn>

Depoorter, M. A., J. L. Bamber, J. A. Griggs, J. T. Lenaerts, S. R. Ligtenberg, M. R. van den Broeke, and G. Moholdt, 2013: Calving fluxes and basal melt rates of Antarctic ice shelves. *Nature*, **502**, 89–92, https://doi.org/10.1038/nature12567.</jrn>

Fair, Z., M. Flanner, K. M. Brunt, H. A. Fricker, and A. Gardner, 2020: Using ICESat-2 and operation icebridge altimetry for supraglacial lake depth retrievals. *Cryosphere*, **14**, 4253–4263, https://doi.org/10.5194/tc-14-4253-2020.

Fanton d'Andon, O., and Coauthors, 2009: GlobColour – The European Service for Ocean Colour. *2009 IEEE Int. Geoscience and Remote Sensing Symp.*, Cape Town, South Africa, IEEE.

Fogt, R. L., Ed., 2011: Antarctica [in "State of the Climate in 2010"]. *Bull. Amer. Meteor. Soc.*, **92** (6), S161–S171, https://doi.org/10.1175/1520-0477-92.6.S1.

Fricker, H. A., and Coauthors, 2021: ICESat-2 meltwater depth estimates: Application to surface melt on Amery ice shelf, East Antarctica. *Geophys. Res. Lett.*, 48, e2020GL090550, https://doi.org/10.1029/2020GL090550.

Frölicher, T. L., J. L. Sarmiento, D. J. Paynter, J. P. Dunne, J. P. Krasting, and M. Winton, 2015: Dominance of the Southern Ocean in anthropogenic carbon and heat uptake in CMIP5 models. *J. Climate*, **28**, 862–886, https://doi.org/10.1175/JCLI-D-14-00117.1.

Gelaro, R., and Coauthors, 2017: The Modern-Era Retrospective Analysis for Research and Applications, version 2 (MERRA-2). *J. Climate*, **30**, 5419–5454, https://doi.org/10.1175/JCLI-D-16-0758.1.

Gloersen, P., 2006: Nimbus-7 SMMR polar gridded radiances and sea ice concentrations, version 1. Subset: 37 & 19 GHz, h-polarization, 25 km grid, Oct 1979–April 1987. NASA National Snow and Ice Data Center Distributed Active Archive Center, accessed 5 May 2020, https://doi.org/10.5067/QOZIVYV-3V9JP.

Gossart, A., S. Helsen, J. T. M. Lenaerts, S. Vanden Broucke, N. P. M. van Lipzig, and N. Souverijns, 2019: An evaluation of surface climatology in state-of-the-art reanalyses over the Antarctic ice sheet. *J. Climate*, **32**, 6899–6915, https://doi.org/10.1175/JCLI-D-19-0030.1.

Gudmundsson, G. H., F. S. Paolo, S. Adusumilli, and H. A. Fricker, 2019: Instantaneous Antarctic ice sheet mass loss driven by thinning ice shelves. *Geophys. Res. Lett.*, **46**, 132903–132909, https://doi.org/10.1029/2019GL085027.

Harvey, N., C. M. McCullough, and H. Save, 2022: Modeling GRACE-FO accelerometer data for the version 04 release. *Adv. Space Res.*, **69**, 1393–1407, https://doi.org/10.1016/j.asr.2021.10.056.

Haumann, F. A., N. Gruber, and M. Münnich, 2020: Sea-ice induced Southern Ocean subsurface warming and surface cooling in a warming climate. *AGU Adv.*, **1**, e2019AV000132, https://doi.org/10.1029/2019AV000132.

Hersbach, H., and Coauthors, 2020: The ERA5 global reanalysis. *Quart. J. Roy. Meteor. Soc.*, **146**, 1999–2049, https://doi.org/10.1002/qj.3803.

Hosking, J. S., A. Orr, G. J. Marshall, J. Turner, and T. Phillips, 2013: The influence of the Amundsen–Bellingshausen Seas low on the climate of West Antarctica and its representation in coupled climate model simulations. *J. Climate*, **26**, 6633–6648, https://doi.org/10.1175/JCLI-D-12-00813.1.

Johnson, A., R. Hock, and M. Fahnestock, 2021: Spatial variability and regional trends of Antarctic ice shelf surface melt duration over 1979–2020 derived from passive microwave data. *J. Glaciol.*, 68, 533–546, https://doi.org/10.1017/jog.2021.11.

Keller, L. M., K. J. Maloney, M. A. Lazzara, D. E. Mikolajczyk, and S. Di Battista, 2022: An investigation of extreme cold events at the South Pole. *J. Climate*, **35**, 1761–1772, https://doi.org/10.1175/JCLI-D-21-0404.1.

Kittel, C., and Coauthors, 2021: Diverging future surface mass balance between the Antarctic ice shelves and grounded ice sheet. *Cryosphere*, **15**, 1215–1236, https://doi.org/10.5194/tc-15-1215-2021.

Kramarova, N., and Coauthors, 2021: 2020 Antarctic ozone hole [in "State of the Climate in 2020"]. *Bull. Amer. Meteor. Soc.*, **102** (8), S345–S349, https://doi.org/10.1175/BAMS-D-21-0081.1.

Kusahara, K., P. Reid, G. D. Williams, R. Massom, and H. Hasumi, 2018: An ocean-sea ice model study of the unprecedented Antarctic sea ice minimum in 2016. *Environ. Res. Lett.*, **13**, 084020, https://doi.org/10.1088/1748-9326/aad624.

Lenaerts, J. T. M., and M. R. Van Den Broeke, 2012: Modeling drifting snow in Antarctica with a regional climate model: 2. Results. *J. Geophys. Res.*, **117**, D05109, https://doi.org/10.1029/2010JD015419.

Li, T., G. Dawson, S. Chuter, and J. Bamber, 2021: A high-resolution Antarctic grounding zone product from ICESat-2 laser altimetry. *Earth Syst. Sci. Data*, **14**, 535–557, https://doi.org/10.5194/essd-14-535-2022.

Ligtenberg, S. R. M., M. M. Helsen, and M. R. Van den Broeke, 2011: An improved semi-empirical model for the densification of Antarctic firn. *Cryosphere*, **5**, 809–819, https://doi.org/10.5194/tc-5-809-2011.

MacFerrin, M., T. Mote, H. Wang, L. Liu, L. Montgomery, and T. Scambos, 2021: Ice sheet seasonal melt extent and duration [in "State of the Climate in 2020"]. *Bull. Amer. Meteor. Soc.*, **102** (8), S331–S334, https://doi.org/10.1175/BAMS-D-21-0081.1.

MacGilchrist, G. A., H. L. Johnson, C. Lique, and D. P. Marshall, 2021: Demons in the North Atlantic: Variability of deep ocean ventilation. *Geophys. Res. Lett.*, **48**, e2020GL092340, https://doi.org/10.1029/2020GL092340.</unknown>

Manney, and Coauthors, 2011: Unprecedented Arctic ozone loss in 2011. *Nature*, **478**, 469–475, https://doi.org/10.1038/nature10556.

Maritorena, S., O. H. Fanton d'Andon, A. Mangin, and D. A. Siegel, 2010: Merged satellite ocean color data products using a bio-optical model: Characteristics, benefits, and issues. *Remote Sens. Environ.*, **114**, 1791–1804, https://doi.org/10.1016/j.rse.2010.04.002.

Marshall, G. J., 2003: Trends in the southern annular mode from observations and reanalyses. *J. Climate*, **16**, 4134–4143, https://doi.org/10.1175/1520-0442(2003)016<4134:TITSAM>2.0.CO;2.

Maslanik, J., and J. Stroeve, 1999: Near-real-time DMSP SSM/I-SSMIS daily polar gridded sea ice concentrations. National Snow and Ice Data Center, accessed 28 March 2022, https://doi.org/10.5067/U8C09DWVX9LM.

Medley, B., and E. R. Thomas, 2019: Increased snowfall over the Antarctic Ice Sheet mitigated twentieth-century sea-level rise. *Nat. Climate Change*, **9**, 34–39, https://doi.org/10.1038/s41558-018-0356-x.

Meehl, G. A., and Coauthors, 2019: Sustained ocean changes contributed to sudden Antarctic sea ice retreat in late 2016. *Nat. Commun.*, **10**, 14, https://doi.org/10.1038/s41467-018-07865-9.

Meier, W. N., H. Wilcox, M. A. Hardman, and J. S. Stewart, 2019: DMSP SSM/I-SSMIS daily polar gridded brightness temperatures, version 5. Subset: 37 & 19 GHz, h-polarization, 25 km grid, Oct 1987–April 2020. NASA National Snow and Ice Data Center Distributed Active Archive Center, accessed 11 February 2021, https://doi.org/10.5067/QU2UYQ6T0B3P.

——, J. S. Stewart, H. Wilcox, M. A. Hardman, and D. J. Scott, 2021: Near-real-time DMSP SSMIS daily polar gridded sea ice concentrations, version 2 [6/1/2021 to 3/27/2022]. NASA National Snow and Ice Data Center Distributed Active Archive Center, accessed 28 March 2022, https://doi.org/10.5067/YTTHO2FJQ97K.

Morlighem, M., and Coauthors, 2020: Deep glacial troughs and stabilizing ridges unveiled beneath the margins of the Antarctic ice sheet. *Nat. Geosci.*, **13**, 132–137, https://doi.org/10.1038/s41561-019-0510-8.

Morrison, A. K., D. W. Waugh, A. McC. Hogg, D. C. Jones, and R. P. Abernathey, 2022: Ventilation of the Southern Ocean pycnocline. *Annu. Rev. Mar. Sci.*, **14**, 405–430, https://doi.org/10.1146/annurev-marine-010419-011012.

Mote, T. L., 2007: Greenland surface melt trends 1973–2007: Evidence of a large increase in 2007. *Geophys. Res. Lett.*, **34**, L22507, https://doi.org/10.1029/2007GL031976.

——, 2014: MEaSUREs Greenland surface melt daily 25km EASE-Grid 2.0, version 1. NASA National Snow and Ice Data Center Distributed Active Archive Center, accessed 30 August 2021, https://doi.org/10.5067/MEASURES/CRYOSPHERE/nsidc-0533.001.

——, and M. R. Anderson, 1995: Variations in snowpack melt on the Greenland ice sheet based on passive microwave measurements. *J. Glaciol.*, **41**, 51–60, https://doi.org/10.1017/S0022143000017755.

Mottram, R., and Coauthors, 2020: What is the surface mass balance of Antarctica? An intercomparison of regional climate model estimates. *Cryosphere*, 15, 3751–3784, https://doi.org/10.5194/tc-15-3751-2021.

NASA, 2022: What is EESC? NASA OzoneWatch, accessed 10 February 2022, https://ozonewatch.gsfc.nasa.gov/facts/eesc_SH.html.

Neckel, N., S. Franke, V. Helm, R. Drews, and D. Jansen, 2021: Evidence of cascading subglacial water flow at Jutulstraumen Glacier (Antarctica) derived From Sentinel-1 and ICESat-2 measurements. *Geophys. Res. Lett.*, **48**, e2021GL094472, https://doi.org/10.1029/2021GL094472.

Neff, W. D., J. Crawford, M. Buhr, J. Nicovich, G. Chen, and D. Davis, 2018: The meteorology and chemistry of high nitrogen oxide concentrations in the stable boundary layer at the south pole. *Atmos. Chem. Phys.*, **18**, 3755–3778, https://doi.org/10.5194/acp-18-3755-2018.

Newman, P. A., J. S. Daniel, D. W. Waugh, and E. R. Nash, 2007: A new formulation of equivalent effective stratospheric chlorine (EESC). *Atmos. Chem. Phys.*, **7**, 4537–4552, https://doi.org/10.5194/acp-7-4537-2007.

Norwegian Polar Institute, 2018: Quantarctica v3.0, detailed basemap. https://www.npolar.no/quantarctica/.

Oliva, M., F. Navarro, F. Hrbáček, A. Hernandéz, D. Nývlt, P. Pereira, J. Ruiz-Fernandéz, and R. Trigo, 2017: Recent regional climate cooling on the Antarctic Peninsula and associated impacts on the cryosphere. *Sci. Total Environ.*, **580**, 210–223, https://doi.org/10.1016/j.scitotenv.2016.12.030.

Orsi, A. H., T. Whitworth III, and W. D. Nowlin Jr., 1995: On the meridional extent and fronts of the Antarctic Circumpolar Current. *Deep-Sea Res. I*, **42**, 641–673, https://doi.org/10.1016/0967-0637(95)00021-W.

Palm, S. P., V. Kayetha, and Y. Yang, 2018: Toward a satellite-derived climatology of blowing snow Over Antarctica. *J. Geophys. Res. Atmos.*, **123**, 102301–102313, https://doi.org/10.1029/2018JD028632.

Paolo, F. S., H. A. Fricker, and L. Padman, 2015: Volume loss from Antarctic ice shelves is accelerating. *Science*, **348**, 327–331, https://doi.org/10.1126/science.aaa0940.

Parkinson, C. L., 2019: A 40-y record reveals gradual Antarctic sea ice increases followed by decreases at rates far exceeding the rates seen in the Arctic. *Proc. Natl. Acad. Sci. USA*, **116**, 142414–142423, https://doi.org/10.1073/pnas.1906556116.

——, and N. E. DiGirolamo, 2021: Sea ice extents continue to set new records: Arctic, Antarctic, and global results. *Remote Sens. Environ.*, **267**, 112753, https://doi.org/10.1016/j.rse.2021.112753.

Pitts, M. C., L. R. Poole, and R. Gonzalez, 2018: Polar stratospheric cloud climatology based on CALIPSO spaceborne lidar measurements from 2006 to 2017. *Atmos. Chem. Phys.*, **18**, 10881–10913, https://doi.org/10.5194/acp-18-10881-2018.

Qu, T., I. Fukumori, and R. A. Fine, 2019: Spin-up of the southern hemisphere super gyre. *J. Geophys. Res. Oceans*, **124**, 154–170, https://doi.org/10.1029/2018JC014391.

Reid, P. A., and R. A. Massom, 2015: Successive Antarctic sea ice extent records during 2012, 2013 & 2014 [in "State of the Climate in 2014"]. *Bull. Amer. Meteor. Soc.*, **96** (7), S163–S164, https://doi.org/10.1175/2015BAMSStateoftheClimate.1.

——, S. Stammerjohn, R. A. Massom, S. Barreira, T. Scambos, and J. Lieser, 2021: Sea ice extent, concentration, and seasonality [in "State of the Climate in 2020"]. *Bull. Amer. Meteor. Soc.*, **102** (8), S336–S338, https://doi.org/10.1175/BAMS-D-21-0081.1.

Reynolds, R. W., N. A. Rayner, T. M. Smith, D. C. Stokes, and W. Wang, 2002: An improved in situ and satellite SST analysis for climate. *J. Climate*, **15**, 1609–1625, https://doi.org/10.1175/1520-0442(2002)015<1609:AIISAS>2.0.CO;2.

Rignot, E., S. Jacobs, J. Mouginot, and B. Scheuchl, 2013: Ice-shelf melting around Antarctica. *Science*, **341**, 266–270, https://doi.org/10.1126/science.1235798.

Roemmich, D., and J. Gilson, 2009: The 2004–2008 mean and annual cycle of temperature, salinity, and steric height in the global ocean from the Argo Program. *Prog. Oceanogr.*, **82**, 81–100, https://doi.org/10.1016/j.pocean.2009.03.004.

Sallée, J. B., K. G. Speer, and S. R. Rintoul, 2010: Zonally asymmetric response of the Southern Ocean mixed-layer depth to the southern annular mode. *Nat. Geosci.*, **3**, 273–279, https://doi.org/10.1038/ngeo812.

Sarmiento, J. L., N. Gruber, M. A. Brzezinski, and J. P. Dunne, 2004: High-latitude controls of thermocline nutrients and low latitude biological productivity. *Nature*, **427**, 56–60, https://doi.org/10.1038/nature02127.

Scambos, T., C. Hulbe, and M. Fahnestock, 2003: Climate-induced ice shelf disintegration in the Antarctic Peninsula. *Antarctic Peninsula Climate Variability: Historical and Paleoenvironmental Perspectives*, E. Domack et al., Eds., Antarctic Research Series, Vol. 79, Amer. Geophys. Union, 79–92, https://doi.org/10.1029/AR079p0079.

——, J. A. Bohlander, C. A. Shuman, and P. Skvarca, 2004: Glacier acceleration and thinning after ice shelf collapse in the Larsen B embayment, Antarctica. *Geophys. Res. Lett.*, **31**, L18402, https://doi.org/10.1029/2004GL020670.

Shepherd, A., and Coauthors, 2012: A reconciled estimate of ice-sheet mass balance. Science, 338, 1183–1189, https://doi.org/10.1126/science.1228102.

Shi, J.-R., S.-P. Xie, and L. D. Talley, 2018: Evolving relative importance of the Southern Ocean and North Atlantic in anthropogenic ocean heat uptake. *J. Climate*, **31**, 7459–7479, https://doi.org/10.1175/JCLI-D-18-0170.1.

——, L. D. Talley, S.-P. Xie, W. Liu, and S. T. Gille, 2020: Effects of buoyancy and wind forcing on Southern Ocean climate change. *J. Climate*, **33**, 10 003–10 020, https://doi.org/10.1175/JCLI-D-19-0877.1.

——, ——, ——, Q. Peng, and W. Liu, 2021: Ocean warming and accelerating Southern Ocean zonal flow. *Nat. Climate Change*, **11**, 1090–1097, https://doi.org/10.1038/s41558-021-01212-5.

Siegfried, M. R., and H. A. Fricker, 2021: Illuminating active subglacial lake processes with ICESat-2 laser altimetry. *Geophys. Res. Lett.*, **48**, e2020GL091089, https://doi.org/10.1029/2020GL091089.

Smith, B., and Coauthors, 2020a: Pervasive ice sheet mass loss reflects competing ocean and atmosphere processes. *Science*, **368**, 1239–1242, https://doi.org/10.1126/science.aaz5845.

——, and Coauthors, 2020b: ATLAS/ICESat-2 L3A land ice height, version 5. NASA National Snow and Ice Data Center Distributed Active Archive Center, accessed 25 January 2022, https://doi.org/10.5067/ATLAS/ATL06.005.

Smith, T. M., R. W. Reynolds, T. C. Peterson, and J. Lawrimore, 2008: Improvements to NOAA's historical merged land–ocean surface temperature analysis (1880–2006). *J. Climate*, **21**, 2283–2296, https://doi.org/10.1175/2007JCLI2100.1.

Song, Y., and W. A. Robinson, 2004: Dynamical mechanisms for stratospheric influences on the troposphere. *J. Atmos. Sci.*, **61**, 1711–1725, https://doi.org/10.1175/1520-0469(2004)061<1711:DMFSIO>2.0.CO;2.

Stammerjohn, S., and T. Maksym, 2017: Gaining (and losing) Antarctic sea ice: Variability, trends and mechanisms. *Sea Ice*, D. N. Thomas, Ed., Wiley, 261–289, https://doi.org/10.1002/9781118778371.ch10.

——, and T. A. Scambos, 2020: Warming reaches the South Pole. *Nat. Climate Change*, **10**, 710–711, https://doi.org/10.1038/s41558-020-0827-8.

——, D. G. Martinson, R. C. Smith, X. Yuan, and D. Rind, 2008: Trends in Antarctic annual sea ice retreat and advance and their relation to El Niño–Southern Oscillation and southern annular mode variability. *J. Geophys. Res.*, **113**, C03S90, https://doi.org/10.1029/2007JC004269.

Stone, K. A., S. Solomon, D. E. Kinnison, and M. J. Mills, 2021: On recent large Antarctic ozone holes and ozone recovery metrics. *Geophys. Res. Lett.*, **48**, e2021GL095232, https://doi.org/10.1029/2021GL095232.

Strahan, S. E., A. R. Douglass, and M. R. Damon, 2019: Why do Antarctic ozone recovery trends vary? *J. Geophys. Res. Atmos.*, **124**, 8837–8850, https://doi.org/10.1029/2019JD030996.

The IMBIE Team, 2018: Mass balance of the Antarctic Ice Sheet from 1992 to 2017. *Nature*, **558**, 219–222, https://doi.org/10.1038/s41586-018-0179-y.

Thompson, D. W. J., J. C. Furtado, and T. G. Shepherd, 2006: On the tropospheric response to anomalous stratospheric wave drag and radiative heating. *J. Atmos. Sci.*, **63**, 2616–2629, https://doi.org/10.1175/JAS3771.1.

Turner, J., T. Phillips, J. S. Hosking, G. J. Marshall, and A. Orr, 2013: The Amundsen Sea low. *Int. J. Climatol.*, **33**, 1818–1829, https://doi.org/10.1002/joc.3558.

——, and Coauthors, 2016: Absence of 21st century warming on Antarctic Peninsula consistent with natural variability. *Nature*, **535**, 411–415, https://doi.org/10.1038/nature18645.

——, and Coauthors, 2019: The dominant role of extreme precipitation events in Antarctic snowfall variability. *Geophys. Res. Lett.*, **46**, 3502–3511, https://doi.org/10.1029/2018GL081517.

Walker, C. C., M. K. Becker, and H. A. Fricker, 2021: A high resolution, three-dimensional view of the D-28 calving event from Amery ice shelf with ICESat-2 and satellite imagery. *Geophys. Res. Lett.*, **48**, e2020GL091200, https://doi.org/10.1029/2020GL091200.

Wang, Y., and Coauthors, 2016: A comparison of Antarctic Ice Sheet surface mass balance from atmospheric climate models and in situ observations. *J. Climate*, **29**, 5317–5337, https://doi.org/10.1175/JCLI-D-15-0642.1.

Warner, R. C., H. A. Fricker, S. Adusumilli, P. Arndt, J. Kingslake, and J. J. Spergel, 2021: Rapid formation of an ice doline on Amery Ice Shelf, East Antarctica. *Geophys. Res. Lett.*, **48**, https://doi.org/10.1029/2020GL091095.

Wiese, D. N., D.-N. Yuan, C. Boening, F. W. Landerer, and M. M. Watkins, 2022: JPL GRACE and GRACE-FO Mascon Ocean, Ice, and Hydrology Equivalent Water Height Coastal Resolution Improvement (CRI) Filtered Release 06 Version 02. PO.DAAC, accessed 25 January 2022, https://doi.org/10.5067/TEMSC-3JC62.

Wild, C. T., K. E. Alley, A. Muto, M. Truffer, T. A. Scambos, and E. C. Pettit, 2022: Weakening of the pinning point buttressing Thwaites Glacier, West Antarctica. *Cryosphere*, **16**, 397–417, https://doi.org/10.5194/tc-16-397-2022.

Wille, J. D., and Coauthors, 2021: Antarctic Atmospheric river climatology and precipitation impacts. *J. Geophys. Res. Atmos.*, **126**, e2020JD033788, https://doi.org/10.1029/2020JD033788.

Yuan, X., 2004: ENSO-related impacts on Antarctic sea ice: A synthesis of phenomenon and mechanisms. *Antarct. Sci.*, **16**, 415–425, https://doi.org/10.1017/S0954102004002238.